UNIVERSITÀ DEGLI STUDI DI ROMA
"TOR VERGATA"

Facoltà di Scienze Matematiche, Fisiche e Naturali

Dipartimento di Fisica

Bunch Length Characterization at the TTF VUV-FEL

Tesi di Dottorato di Ricerca in Fisica

Enrica Chiadroni

Relatore:
Prof. *Sergio Tazzari*

Relatore:
Dott. *Michele Castellano*

Coordinatore del Dottorato:
Prof. *Piergiorgio Picozza*

Ciclo XVIII

Anno Accademico 2004-2005

TESLA-FEL 2006-09

To my dear granny, illiterate and almost hundred-year-old...

Contents

List of Figures

List of Tables

Abstract

The characterization of the longitudinal density profile or bunch shape of picosecond and sub-picosecond relativistic particle bunches is a fundamental requirement in many particle accelerator facilities, since knowledge of the characteristics of the accelerated beams is of utmost importance for the successful development of the next generation light sources and linear colliders. The development of suitable beam diagnostics, non-invasive and non-intercepting, is thus necessary to produce and control such beams. First experimental evidences of the non-intercepting and non-destructive nature of DR diagnostics are presented.

The precise longitudinal bunch distributions downstream of the second bunch compressor (DBC3) of the DESY TTF VUV-FEL have been reconstructed using a frequency-domain technique based on the autocorrelation of coherent diffraction radiation (CDR). A Kramers-Kronig analysis has then been applied to derive the minimal phase.

The autocorrelation of diffraction radiation coming from a thin conducting foil placed in the vacuum chamber has been obtained using a Martin-Puplett interferometer and sub-millimeter radiation.

The measurement and the reconstruction of the longitudinal bunch distribution are discussed in detail showing also the strong dependence of the bunch length on the accelerating module phase.

Due to the low and high frequency suppression, introduced by the experimental apparatus, only a portion of the CDR spectrum participates to the reconstruction of the longitudinal bunch profile. The knowledge of the system frequency response, in particular in the millimeter and sub-millimeter range is then crucial in order to correct the results and extrapolate a bunch shape as close as possible to the real one. At this purpose, a precise characterization over three different frequency regions of the Golay cell detector used for the measurement is also discussed, thus extending the cell calibration into the long wavelengths region.

Outline

The PhD thesis has been developed at the DESY VUV-FEL in the framework of the SPARC collaboration, with the purpose of both transferring the know-how and sharing hardware of the bunch length measurement at SPARC. The measurement is planned to be performed in the SPARC phase 2, when the installation and operation of the bunch compressor is foreseen, being the bunch length too long (2 mm) for the interferometer technique to be applied in the early operation.

The thesis is organized as follows. The first chapter is a brief overview of the FEL principle of operation, ultra-high brilliance electron beams (high peak current, small transverse emittance) being highly required for the production of FEL radiation. The theory background concerning the bunch length measurement, radiation source and data analysis is treated in chapter 2. Chapter 3 illustrates the experimental apparatus used to measure the bunch length and gives a detailed description of the detecting system, including the detector frequency response up to few millimeters. Finally the bunch length characterization is given in chapter 4 where experimental data are discussed.

Appendix sections are dedicated to VUV-FEL and SPARC machine parameters (appendix A), transmission of the millimeter wave materials (appendix B), details on the calibration of the Golay cell detector (appendix C) and quantitative approach to Fourier transform spectroscopy (appendix D).

Chapter 1

Introduction

The characterization of electron beams is of primary interest in many particle accelerator facilities, since a detailed knowledge of either transverse or longitudinal size of particle beams is much needed for the successful development of the next generation light sources, i.e. Free-Electron Lasers (FEL) [1], [2], [3] and new generation linear colliders [4]. The development of suitable beam diagnostics is thus necessary to produce and control such beams.

The longitudinal bunch distribution downstream of the second bunch compressor, named DBC3, at the DESY Tesla Test Facility Vacuum Ultraviolet Free-Electron Laser (TTF VUV-FEL) has been reconstructed using a frequency-domain technique [5] based on the autocorrelation of coherent diffraction radiation (CDR). An overview of the TTF VUV-FEL is given in section 1.2 and a more detailed description of its injector and the two magnetic compressors involved in this work is reported in chapter 3.1.

A Martin-Puplett interferometer is used to obtain the autocorrelation of coherent diffraction radiation in the sub-millimeter wavelength range coming from a thin conducting foil placed in the vacuum chamber. The diffraction radiation theory from both an infinite and a finite size target, in the far-field and near-field approximation, is described in chapter 2, where the theory of coherent radiation diagnostics is also presented.

Limits of a frequency domain technique for bunches whose shape is not well known and ideas about how to overcome them are discussed.

Precise characterization over three different frequency regions of the Golay cell detector used for the measurement is also discussed in chapter 3.5, giving for the first-time a calibration of such a cell in the mm-wavelength

region.

1.1 FEL Basic Principle

As already pointed out, short bunches with high peak current, together with small relative energy spread ($\frac{\Delta\gamma}{\gamma}$) and small normalized transverse emittance[1] (ε_n), are fundamental features to be reached and preserved during operation of electron beams driving Free-Electron Lasers.

In this section, we shall summarize the FEL working principle and discuss how these parameters are related to the FEL gain length[2] $L_g = \frac{\lambda_u}{4\pi\sqrt{3}\rho}$ (λ_u and ρ are defined later), power P and radiation wavelength λ_r.

The main difference between a Free-Electron Laser and a conventional laser is the gain medium. In a FEL electrons are not bound to the quantum states of an optical medium, but to a magnetic device, the undulator, shown in figure 1.1.

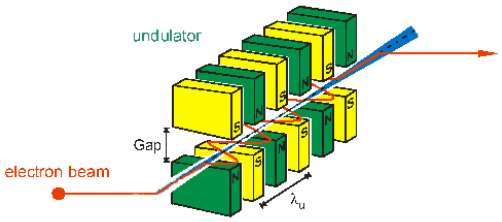

Figure 1.1: Sketch of the undulator.

Electrons, forced by the undulator magnetic field to oscillate transversely to the direction of propagation, emit the so-called undulator spontaneous radiation, which shows a sharp peak when the resonance condition

$$\lambda_r = \frac{\lambda_u}{2\gamma^2}\left(1 + \frac{K^2}{2}\right) \tag{1.1}$$

[1]The normalized transverse emittance, $\varepsilon_n = \gamma\varepsilon_g$, is the area, corrected by the electron Lorentz factor, occupied by the beam in the 2D transverse phase space, ε_g being the geometric emittance. It is typically measured in units of π *mm mrad* (size x angular divergence).

[2]In the 1D FEL theory, it is defined as the length necessary to the radiation field to be increased of e, the Napier's constant.

is satisfied, λ_u being the undulator period, γ the electron beam Lorentz factor and K the undulator parameter. The latter, defined as $K = \frac{eB_0\lambda_u}{2\pi m_0 c^2}$ where B_0 is the maximum amplitude of the magnetic field and m_0 the electron mass, is a measure of the on-axis undulator magnetic field once the undulator period is fixed.

In a Self-Amplified Spontaneous Emission (SASE) FEL, the undulator spontaneous radiation is the seed from which the emission of stimulated radiation grows. The FEL gain, proportional to the electron peak current, is maximized by compressing the electron beam at relatively high energy so that transverse and longitudinal space charge forces are negligible[3]. The bunch compression is performed by introducing an energy deviation, correlated with the longitudinal position z in the bunch and then passing the bunch through a magnetic system where the path length is energy dependent. Compression increases both the peak current and, because the longitudinal emittance[4] ε_L is conserved, the energy spread.

Figure 1.2 shows the dependence of gain length on current [6]. The increase in peak current produces a significant reduction of the gain length, resulting in a shorter FEL saturation length. The increase in peak current has to be balanced thus against the increase in the beam energy spread.

Finally, during acceleration to high energy and compression of the beam, the beam emittance has to be preserved and delivered to the undulator. However, the requirements for lasing on the emittance and energy spread only need to be maintained over a distance λ_r/ρ, called cooperation length, much shorter than the bunch length; ρ being the dimensionless FEL parameter, typically of the order of 10^{-3}. The transverse emittance integrated over a distance of the order of the cooperation length is then called *slice* emittance.

The relation between these quantities and the FEL main parameters is given by [7] through the following scaling laws (Eq. 1.2) showing the key role

[3]In the accelerator straight sections, space charge forces on the bunch scale linearly with the beam current (with given transverse dimensions) and inversely with the square of the beam energy ($\frac{I}{\gamma^2}$), while in bending magnet systems, such as bunch compressors, they scale like $(\frac{\sigma_x}{R})^{3/2}$, where σ_x is the beam size and R the bending radius.

[4]It is defined as the area, divided by π, of the ellipse in the longitudinal phase space. Choosing as longitudinal phase space variables the RF phase, ϕ, and the relative momentum spread, $\frac{\Delta p}{p}$, which is assumed to be equal to the relative energy spread, $\frac{\Delta E}{E}$, for ultra-relativistic beams, the rms longitudinal emittance is defined as $\varepsilon_L = \sqrt{< \phi^2 >< (\frac{\Delta p}{p})^2 > - < \phi \frac{\Delta p}{p} >^2}$.

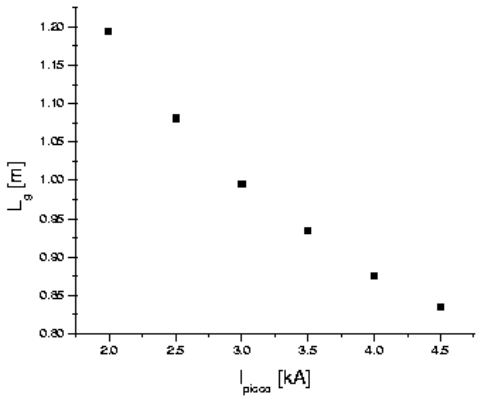

Figure 1.2: Gain length as function of the electron beam peak current (Simulation with GENESIS 1.3). Beam parameters: $E_e = 2\ GeV$, $\lambda_r = 10\ nm$, $\varepsilon_n(slice) = 1\ \pi\ mm\ mrad$, $\frac{\Delta\gamma}{\gamma} = 0.1\%$.

of $\frac{\Delta\gamma}{\gamma}$ and ε_n in order to get short radiation wavelength in few gain lengths:

$$\lambda_{r,cr} \propto \frac{\varepsilon_n}{\gamma}\frac{\Delta\gamma}{\gamma}I^{-1/2} \tag{1.2}$$

$$L_{g,cr} \propto \frac{\varepsilon_n}{\gamma}\gamma^{5/2}I^{-1/2} \tag{1.3}$$

$$P \propto \exp(\frac{z}{L_g}) \tag{1.4}$$

Equation (1.2) shows a linear dependence of the radiation wavelength, $\lambda_{r,cr}$, on both relative energy spread and transverse emittance, and on the peak current as $I^{-1/2}$. Since neither ε_n nor $\frac{\Delta\gamma}{\gamma}$ can be reduced indefinitely to get wavelengths in the range of VUV-X, a peak current of the order of kA and electron beam energy of the order of a GeV are required.

1.2 The TTF VUV-FEL

The TESLA Test Facility (TTF) has been designed and built to produce an electron beam of extremely high quality in terms of emittance, energy spread and peak current. The TTF-Phase2 linac has been upgraded to drive

a SASE FEL facility, named VUV-FEL [8], and is shown in Fig. 1.3. An overview of the expected FEL parameters both in the short wavelength and in the present operation mode of the TTF VUV-FEL is given in appendix A.

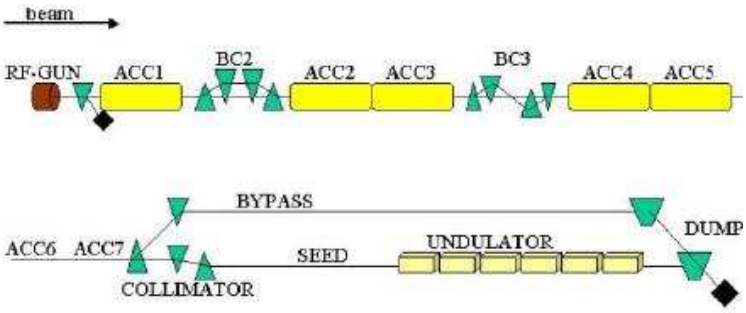

Figure 1.3: Sketch of the VUV-FEL boost.

Electron bunch trains of up to 4 nC charge and repetition rate of up to 5 Hz are generated by a laser-driven radio-frequency (RF) photocathode electron gun, the bunch repetition rate being 1 MHz. In order to reduce space charge effects, the laser pulse shape should ideally be rectangular, both transversely and longitudinally, having a length of 20 ps (FWHM). The design rms bunch length at the gun exit is 2.2 mm. Before entering the undulator, composed of six 5 m long sections, the beam passes through seven accelerating modules each consisting of eight nine-cell superconducting 1.8 K niobium RF cavities operating at 1.3 GHz and two bunch compressors (named BC2 and BC3 for historical reasons). The last two modules, ACC6 and ACC7 are needed to reach the design electron energy of 1 GeV.

At present, electrons are accelerated to an energy of 127 MeV in the first module (ACC1) and pass through the first bunch compressor (BC2) where the bunch is shortened by a factor of up to eight. Downstream from BC2, modules ACC2 and ACC3 increase the energy to 380 MeV and the bunch undergoes a second compression (BC3) by a factor of up to five. In Chapter 4, the strong dependence of the bunch size on the accelerating RF phase will be shown.

Our experimental setup is placed immediately downstream from BC3. Details on experimental components and techniques, e.g. diffraction radiator, vacuum window, interferometer components and their alignment, are given in Chapter 3.

1.3 Different techniques to measure the bunch length

Along the whole TTF tunnel several experiments based on coherent radiation diagnostics [9] using different radiation sources, e.g. synchrotron, transition and diffraction radiation, are installed and the spectral distribution of the radiation is measured with various instruments, for example Martin-Puplett interferometers or grating spectrometers. However, since none of them allow the bunch shape to be fully reconstructed due to the ambiguity of the inversion process, several other, possibly more powerful devices mostly in the time domain are also being investigated at the VUV-FEL: the streak camera, the LOLA[5] deflecting cavity and the electro-optical sampler (EOS) [10].

The main advantage of a time domain method is due to the fact it is directly sensitive to the longitudinal charge distribution. The most well-known one is the streak camera which though, because of its 1 *ps* resolution limit, is inadequate for sub-ps long bunches. The LOLA experiment uses a transverse RF mode in a cavity to separate the head from the tail of a bunch: the deflecting structure imparts a transverse kick to the particles within the bunch which results in a transverse offset observed on an optical transition radiation (OTR) screen. The technique has though the drawback of being invasive. EOS is instead non-invasive and therefore much more suitable. It uses the dependence of the birefringence of a non-linear crystal on the strength of an external electric field. The superposition of a laser pulse, triggered by the arrival on the bunch generated CTR produces a detectable rotation of the laser polarization. The polarization information is then transformed in intensity information by means of optical elements traversed by the laser beam. The size of the EOS signal depends on the energy of the coherent transition radiation (CTR) pulse, the crystal orientation and the orientation of the polarization planes of the incoming CTR and laser radiations.

In the present work, a frequency domain technique based on the analysis of the far-infrared radiation (FIR) spectrum of coherent diffraction radiation (CDR) has been used to measure the bunch length. Our choice to use a DR source makes even a frequency domain technique a non-invasive and non-intercepting diagnostics. Measurements during standard FEL operation were indeed performed as shown in chapter 4. The drawback due to the ambiguous reconstruction of the form factor cannot be completely overcome, even

[5]The name comes from its designers: Greg **LO**ew, Rudy **L**arsen and Otto **A**ltenmueller. It was built at SLAC in 1968.

though the spectrum is calculated taking into account the transfer functions of each component in the setup. However, its main deficiency is the ambiguity of retrieving the bunch profile from the measured CDR spectrum, since only the square of the Fourier transform of the longitudinal beam profile can be evaluated, getting no information on the phase. A Kramers-Kronig analysis has to be applied, allowing to find the minimum phase value consistent with the measured module [11].

Contrary to [12] whose main purpose was to demonstrate that CDR can be effectively used as electron beam diagnostics, the present work wants to provide a complete characterization of the electron beam longitudinal profile by taking into account factors, such as the detector frequency response, which influence the profile reconstruction. At this purpose a detailed detector calibration has been performed and presented in chapter 3. Results from the detector calibration have been presented to the FEL Conference 2005.

Chapter 2

Theory

The theory background concerning the bunch length measurement, radiation source and data analysis is treated in the present chapter. First an overview of the emission and propagation mechanisms of radiation for ultra-relativistic particles is given and the transition and diffraction radiation spectra for both single-particle emission and emission from an electron bunch are discussed, showing how information on the bunch longitudinal dimension can be inferred from them. The theoretical approach to the data analysis and the reconstruction of the electron bunch profile is also discussed, based on the Kramers-Kronig dispersion relation, which takes advantage of the analogy with the input-output response function analysis and allows to express the real part of any spectral function as an integral involving the imaginary part (and vice-versa).

2.1 Diffraction Radiation

Many relativistic emission processes might be used for electron beam diagnostics, i.e. synchrotron radiation, Cherenkov radiation, Smith-Purcell radiation [13], transition and diffraction radiation, the last two being considered two aspects of the same phenomenon. Radiation is produced when a charged particle crosses the discontinuity between two media both directly (transition radiation, TR) and at a distance close to the edge of a metallic screen (diffraction radiation, DR), if the distance, ρ, to the target is such that

$$\rho \leq \frac{\gamma\lambda}{2\pi} \tag{2.1}$$

λ being the emitted radiation wavelength depending on diffractive effects and γ the electron Lorentz factor showing the Lorentz transformations of electromagnetic fields.

The radiation produced is due to the presence of optical inhomogeneities in the space, where the field of travelling charge induces, on the target surface, currents changing in time, and these currents generate radiation.

The TR process was calculated analytically by solving the Maxwell equations in the assumptions of infinite size target, infinitely thin and ideally flat, perfectly conducting material and far-field approximation, by Ginzburg-Frank, the spectral and spatial energy distribution from a single electron being described by the formula [14]

$$\frac{d^2U}{d\omega d\Omega} = \frac{e^2}{4\pi^3\varepsilon_0 c}\frac{\beta^2\sin^2\vartheta}{(1-\beta^2\cos^2\vartheta)^2} \tag{2.2}$$

with $\beta = \frac{v}{c}$ and ϑ the observation angle. The angular distribution is shown in Fig. 2.1, where a feature, characteristic of radiation emitted by an accelerated charge in ultra-relativistic motion, is evident, the intensity being zero at $\vartheta = 0$ and maximum at $\vartheta \simeq \frac{1}{\gamma}$ for $\gamma \gg 1$.

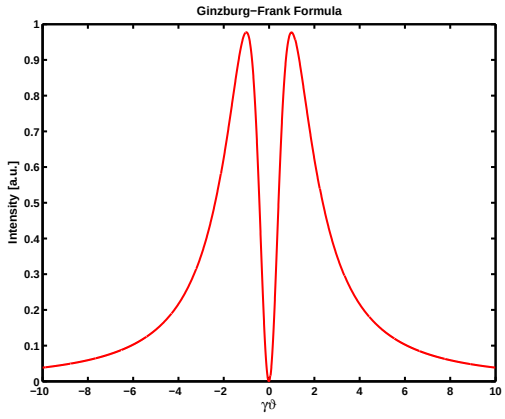

Figure 2.1: Angular distribution of the TR intensity according to the Ginzburg-Frank formula.

Furthermore, for frequencies well below the plasma frequency, ω_p, of the metal and in the limits of validity of the Ginzburg-Frank formula, the spectral distribution of TR radiation does not depend on the frequency. In the following sections, we will see that in practice the assumptions of infinite size

target and far-field approximation are not fulfilled, causing the spectrum be frequency-dependent [15].

TR, as DR, has the tendency to propagate in two main directions along the trajectory of the particle, in the forward direction (forward transition or diffraction radiation, FTR or FDR) and in the backward direction (backward transition or diffraction radiation, BTR or BDR), within a cone whose axis is coincident with the direction of propagation of the particle and with angular aperture proportional to $\frac{1}{\gamma}$. In case the target is oriented with angle θ_0 with respect to the direction of the incident particle, the backward radiation propagates in the direction of the mirror reflection. The $\theta_0 = 45^o$ geometry (Fig. 2.2) is the most suitable one from the experimental point of view since the emitted radiation is well separated from the electron beam, being orthogonal to the direction of the particle velocity. Furthermore, for ultra-relativistic particles the two lobes at 45^o with respect to each other do not overlap, resulting in independent angular distributions.

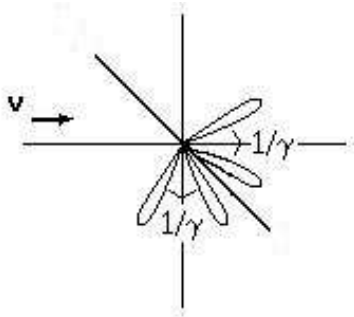

Figure 2.2: Emission geometry for a target tilted with a 45 angle.

Assuming a highly conducting, reflecting surface and $\gamma \gg 1$, the angular distributions of the radiation emitted in both cases, normal and 45^o incidence target with respect to the direction of propagation, are similar and we are allowed to assume the finite size target oriented at 45^o equivalent to the one placed at 90^o with respect to the beam line whose horizontal dimension l becomes $l \sin(\theta_0)$.

In case of DR produced by a charged particle passing exactly in the middle of an aperture in a metallic screen, no radiation is emitted at $\theta = 0$ and the angular distribution is similar to the TR one. For this reason, DR can be treated as TR emitted by a surface with a cut on it which gives rise to a diffraction pattern. For the Babinet principle[1], the DR spectrum can be

[1]The diffraction fields of a diffracting screen are equivalent to those of the complemen-

therefore deduced by simply subtracting from the TR spectrum for a target of size b, the TR spectrum for a target of size $a < b$.

Beyond the simple emission geometry, DR allows a non-intercepting and non-invasive diagnostics, the great interest in this type of radiation coming also from both the possibility of generation of intense radiation beams in millimeter and sub-millimeter wavelength region and beam diagnostics based on both incoherent and coherent diffraction radiation. In section 2.2 we will discuss about the information we can obtain on the electron bunch structure by studying coherent radiation, independently on the source used.

In the following subsections we will first introduce the radiation mechanism of ultra-relativistic particles, then derive the single-particle spectrum from both a slit in an infinite size target and a rectangular aperture in a finite size rectangular target. In the case of circular geometry, the mathematical derivation can be performed analytically only for the case of the particle going exactly through the center of the hole, the formula being extremely complicate otherwise. For this reason and because the mechanical manufacture is more precise for a slit than a hole, the rectangular geometry has been preferred.

2.1.1 Virtual Photon Method

The radiation emission mechanism can be described with the Weizsäcker-Williams method or virtual photon method [16], the essence of the method being the replacement of the particle field by the field of a plane wave.

Consider an electron, e, which moves uniformly with velocity $\vec{v}$ along the z-axis; let denote K' its rest reference system and K the system solidal with an observer located at the point $P \equiv (0, \rho, 0)$ from the charge (Fig. 2.3).

The fields corresponding to a boost along the z-axis with speed βc from K to K' are transformed by means of Lorentz transformations so that

$$\begin{aligned} E'_x &= \gamma(E_x + \beta B_y) & B'_x &= \gamma(B_x + \beta E_y) \\ E'_y &= \gamma(E_y - \beta B_x) & B'_y &= \gamma(B_y - \beta E_x) \\ E'_z &= E_z & B'_z &= B_z \end{aligned} \tag{2.3}$$

γ being the electron Lorentz factor.

At $t = t' = 0$, the origins of the two coordinate systems coincide. The

tary screen.

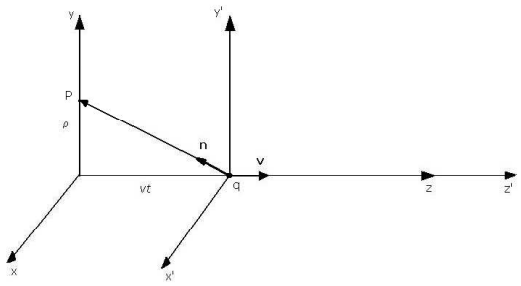

Figure 2.3: Inertial frames for the evaluation of the electromagnetic field for a particle of charge q moving with constant velocity $\vec{v}$ along the z-axis.

point P in the system K', where the fields must be evaluated, has coordinates

$$\begin{aligned} x' &= x = 0 \\ y' &= y = \rho \\ z' &= \gamma(z - vt) = -\gamma vt \\ t' &= \gamma(t - \frac{v}{c^2}z) = \gamma t \end{aligned}$$

the distance to the source being $r' = \sqrt{x'^2 + y'^2 + z'^2} = \sqrt{\rho^2 + \gamma^2 v^2 t^2}$. In the rest frame K' of the electron, the electric and magnetic fields at the observation point are given by [14]

$$\begin{aligned} E'_x &= 0 & B'_x &= 0 \\ E'_y &= \frac{e}{4\pi\varepsilon_0}\frac{\rho}{(\rho^2 + v^2t^2\gamma^2)^{3/2}} & B'_y &= 0 \\ E'_z &= -\gamma\frac{e}{4\pi\varepsilon_0}\frac{evt}{(\rho^2 + v^2t^2\gamma^2)^{3/2}} & B'_z &= 0 \end{aligned} \tag{2.4}$$

The transformed fields in the observer reference system K are therefore obtained by using the inverse of 2.3 so that the non-vanishing components are

$$\begin{aligned} E_y &= \gamma E'_y = \frac{e}{4\pi\varepsilon_0}\frac{\gamma\rho}{(\rho^2 + v^2t^2\gamma^2)^{3/2}} \\ E_z &= E'_z = -\frac{e}{4\pi\varepsilon_0}\frac{e\gamma vt}{(\rho^2 + v^2t^2\gamma^2)^{3/2}} \\ B_x &= \gamma\beta E'_y = \beta E_y \end{aligned} \tag{2.5}$$

Equations 2.5 show the main difference between the electromagnetic field of a particle and that from light waves: the latter being transverse, while the former has a component of the electric field always directed along $\vec{v}$.

However, for ultra-relativistic particles ($\gamma \gg 1$), whose velocity tends to the speed of light, $v \to c$, the electromagnetic field of a particle acquires the properties of electromagnetic waves. Denoting with E_p and E_n the components of the electric field parallel (E_z) and normal (E_y) to the direction of motion, respectively, figure 2.4 shows how as γ increases, the peak fields increase proportionally, their duration though going in inverse proportion. The time interval over which the fields are appreciable is $\Delta t \simeq \frac{\rho}{\gamma v}$, where ρ, called impact parameter, is the distance of the particle to the obstacle. Figure 2.4 shows also that in the transverse direction, the field strength is

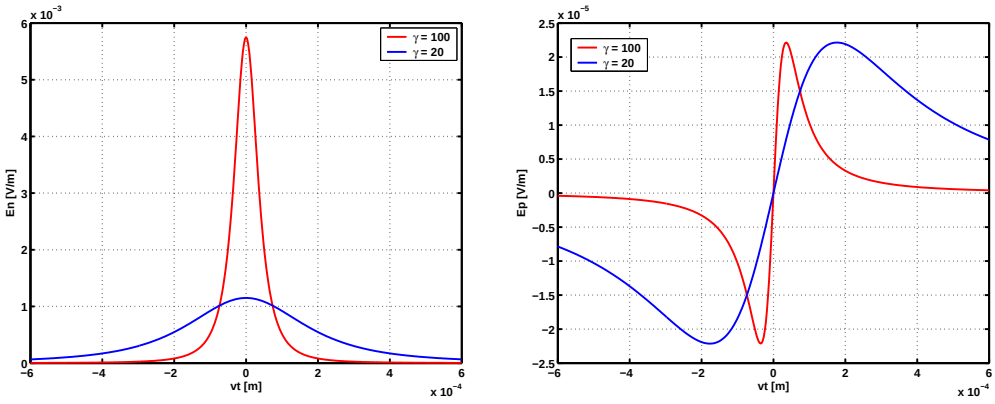

(a) $E_n \perp v$ (b) $E_p \parallel v$

Figure 2.4: Electric fields at the observation point P as a function of time.

larger than the longitudinal component by a factor of γ, which confirms the replacement of the particle field by the field of the light waves.

The harmonic content of the electron field varying in time is obtained by Fourier transforming the radial electric field, $\vec{E}$, at the position of the radiator, $z = 0$ (Eq. 2.6) and with the assumption $E_p \ll E_n$, the longitudinal field component can be neglected,

$$\begin{aligned} E_n(\omega) &= \gamma \frac{e}{4\pi\varepsilon_0} \frac{\rho}{2\pi} \int_{-\infty}^{\infty} \frac{e^{-i\omega t} dt}{(\rho^2 + v^2 t^2 \gamma^2)^{3/2}} \\ &= \frac{e\omega}{(2\pi)^{3/2} \varepsilon_0 \gamma v^2} K_1\left(\frac{\rho\omega}{\gamma v}\right) \end{aligned} \tag{2.6}$$

K_1 being the modified Bessel function. The electric field transverse component is then proportional to $\frac{\rho\omega}{\gamma v} K_1(\frac{\rho\omega}{\gamma v})$, whose width at half maximum is roughly 0.6 for the argument equal to 1, as shown in Fig. 2.5, where the function $xK_1(x)$ is plotted.

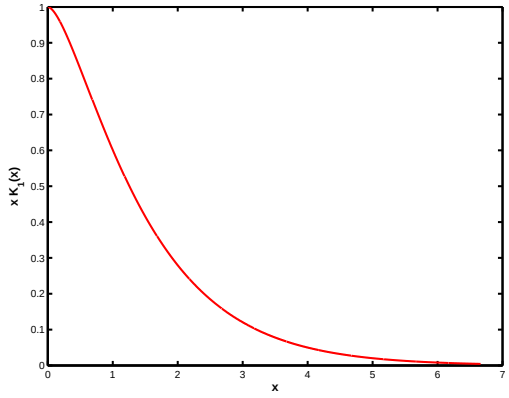

Figure 2.5: Modified Bessel function of second order.

Recalling that $v = \beta c$ and $\omega = \frac{2\pi c}{\lambda}$ and assuming $\beta \sim 1$, a strong field is detected and radiation emitted if the following condition is satisfied

$$\frac{\rho\omega}{\gamma v} < 1 \Leftrightarrow \rho \leq \frac{\gamma\lambda}{2\pi} \tag{2.7}$$

Radiation is therefore confined within a disk of radius $\gamma\lambda$. Contrary to the plane electromagnetic wave, the particle field depends on the distance from it (Eq. 2.7). This result gives also an idea of the application limits of the infinite size condition, whose consequences are the topic of the following subsections.

2.1.2 Diffraction Radiation from a Slit between Two Semi-Planes

As introduced in the previous subsection, for fast particles the particle field becomes equivalent to a set of plane waves, allowing the electromagnetic field of the travelling particle to be expressed by the field of virtual photons. The transition or diffraction radiation field can therefore be considered as the scattering of the virtual photons field due to the target. The radiated energy is determined by solving the Kirchoff integral [18] which, in the far-field approximation, can be considered as the Fourier transform on the target surface of the field of virtual photons.

Consider an electron, moving uniformly along the z-axis with velocity $v \to c$ passing through a slit, whose edge is parallel to the x-axis, between

two semi-planes, assumed to be flat, absolutely opaque and infinitely thin (Fig. 2.6). The electron trajectory is perpendicular to the plane of the target coinciding with the plane xy.

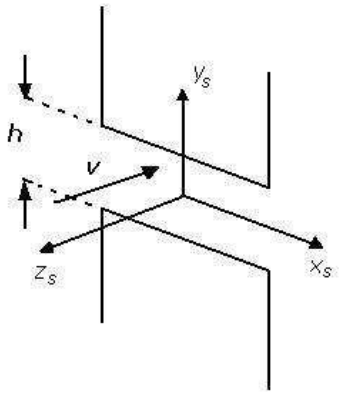

Figure 2.6: Sketch of the electron passing through an aperture in an infinite size target.

The diffraction radiation field from a slit between the two semi-planes can then be obtained from the Huygens-Fresnel integral over the area $S_2 = S_\infty - S_1$, calculated from a thin, ideal conducting metal screen of infinite extent S_∞ on which a slit of material of area S_1 is removed. The DR field can then be expressed as [16]

$$E(\omega) = -\frac{1}{(2\pi)^2}\int_{S_2}\frac{E^0(x_s,y_s)}{R'}e^{i\frac{\omega}{c}R'}dS \tag{2.8}$$

with $R' = \sqrt{D^2+(x-x_s)^2+(y-y_s)^2}$ the distance from an element of the emitting area, $dS = dx_s dy_s$, to the point P (see Fig. 2.7). The incident field, $\vec{E}^0$, is the field associated to the relativistic particle travelling uniformly along the z-axis and given by the expression

$$E^0_{x,y}(x_s,y_s) = -\frac{ie}{2\pi v^2}e^{i\frac{\omega}{v}z}\int\frac{\kappa_{x,y}e^{i(\kappa_x x_s+\kappa_y y_s)}}{\kappa_x^2+\kappa_y^2+\alpha^2}d\kappa_x d\kappa_y \tag{2.9}$$

κ_x, κ_y being the projections of the photon vector $\vec{k}$ on the xy plane and $\alpha = \frac{\omega}{\gamma v}$. Expression 2.9 is equivalent to the one (Eq. 2.6) found in the previous subsection.

The origin of coordinates is chosen at the intersection point between the particle trajectory and the slit plane. R' can then be written, as long as R

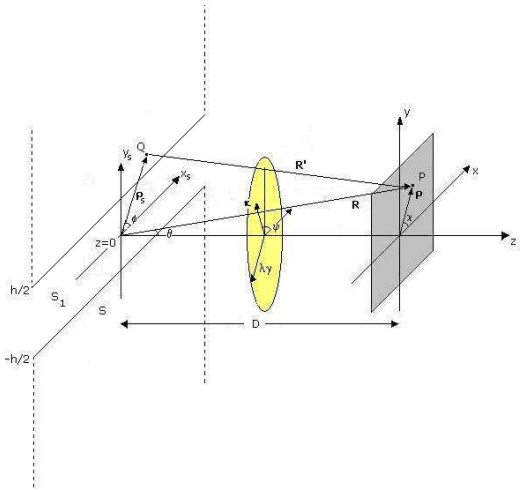

Figure 2.7: Diffraction radiation geometry.

is much larger than the aperture dimensions, as

$$\begin{aligned} R' &= \sqrt{D^2 + x^2 + y^2 + x_s^2 + y_s^2 - 2(xx_s + yy_s)} \\ &= R\sqrt{1 + \frac{\rho_s^2}{R^2} - 2\frac{\hat{n}\cdot\vec{\rho_s}}{R}} \\ &\simeq R - \hat{n}\cdot\rho_s + \frac{\rho_s^2}{2R} \end{aligned} \tag{2.10}$$

with $R^2 = D^2 + x^2 + y^2$ and $\rho_s^2 = x_s^2 + y_s^2$, $\hat{n}$ is the unit vector in the direction of R. The total field at the point P becomes

$$E(P,\omega) = -\frac{e^{i\frac{\omega}{c}R}}{(2\pi)^2}\int_{S_2} E^0(x_s,y_s)e^{-i\vec{k}\cdot\vec{\rho_s}}e^{i\frac{\omega}{c}\frac{\rho_s^2}{2R}}dS \tag{2.11}$$

where $\vec{k} = \frac{\omega}{c}\hat{n}$ is the photon wave vector. The phase factor proportional to ρ_s is of Fraunhofer type and is responsible for fields at far distance from the source, while the one depending on ρ_s^2 is the first order Fresnel correction to the far-field approximation. In what follows, we will assume valid the Fraunhofer approximation, the DR field being expressed by

$$E(P,\omega) = -\frac{1}{(2\pi)^2}\int_{S_2} E^0(x_s,y_s)e^{-i\vec{k}\cdot\vec{\rho_s}}dS \tag{2.12}$$

Let assume the particle is moving exactly in the middle of the aperture, at a distance $\frac{h}{2}$ from the origin of coordinates to the slit edges; substituting

Eq. 2.9 in Eq. 2.12 and integrating the field parallel to edge, for example, over x from $-\infty$ to ∞ and over y from $-\infty$ to $-\frac{h}{2}$ and from $\frac{h}{2}$ to ∞, we obtain

$$\begin{aligned} E_x(k_x,k_y) &= \frac{1}{(2\pi)^2}\frac{ie}{2\pi v^2}\Big[\int_{-\infty}^{\infty} dy_s - \int_{-\frac{h}{2}}^{\frac{h}{2}} dy_s\Big] \\ &\int_{-\infty}^{+\infty} dx_s e^{-i(k_x x_s + k_y y_s)} e^{i(\kappa_x x_s + \kappa_y y_s)} \\ &\int_0^{\infty} \frac{\kappa_x}{\kappa_x^2+\kappa_y^2+\alpha^2} d\kappa_x d\kappa_y \end{aligned} \tag{2.13}$$

the integral over y being written as the sum of two integrals: from $-\infty$ to ∞ and from $-\frac{h}{2}$ to $\frac{h}{2}$. Furthermore the integrals over dx_s and dy_s are "a variabili separabili", Eq. 2.13 can then be written as

$$\begin{aligned} E_x(k_x,k_y) \propto & \Big[\int_{-\infty}^{\infty} dy_s e^{-iy_s(k_y-\kappa_y)} - \int_{-\frac{h}{2}}^{\frac{h}{2}} dy_s e^{-iy_s(k_y-\kappa_y)}\Big] \\ & \int_{-\infty}^{+\infty} dx_s e^{-ix_s(k_x-\kappa_x)} \int_0^{k} \frac{\kappa_x d\kappa_x d\kappa_y}{\kappa_x^2+\kappa_y^2+\alpha^2} \end{aligned} \tag{2.14}$$

the integral over dx_s and dy_s from $-\infty$ to ∞ being δ-functions, whose contribution is different from zero if and only if $\kappa_{x,y} = k_{x,y}$, and the integral over the vertical slit aperture is the typical $\frac{\sin x}{x}$ function. $E_x(k_x,k_y)$ can then be written as

$$\begin{aligned} E_x(k_x,k_y) \propto & \int_{-\infty}^{\infty} \frac{k_x}{\kappa_y^2+f^2} \frac{[\sin\frac{h}{2}(k_y-\kappa_y)]}{(k_y-\kappa_y)} d\kappa_y + \\ & + \frac{k_x}{k_x^2+k_y^2+\alpha^2} \end{aligned} \tag{2.15}$$

with $f = \sqrt{k_x^2+\alpha^2}$. Finally, the fields of radiation emitted by an electron moving through a slit in a perfectly conducting, infinite screen and in the Fraunhofer approximation are found by considering the function analytic extension to the complex plane where the integral has three poles at $\kappa_y = \pm if$ and $\kappa_y = k_y$, so that applying the residual theorem [17], the expression for the parallel polarization, as well as for the orthogonal one, have the form

$$\begin{aligned} E_x(k_x,k_y) &= \frac{iek_x}{4\pi^2 cf}\Big\{\frac{e^{-\frac{h}{2}(f-ik_y)}}{f-ik_y} + \frac{e^{-\frac{h}{2}(f+ik_y)}}{f+ik_y}\Big\} \\ E_y(k_x,k_y) &= \frac{e}{4\pi^2 c}\Big\{\frac{e^{-\frac{h}{2}(f-ik_y)}}{f-ik_y} - \frac{e^{-\frac{h}{2}(f+ik_y)}}{f+ik_y}\Big\} \end{aligned} \tag{2.16}$$

where $k_x = k \sin\theta \cos\phi$, $k_y = k \sin\theta \sin\phi$, θ and ϕ being the polar and azimuthal angle of radiation.

The DR spectral angular distribution is then

$$\begin{aligned} \frac{d^2U}{d\omega d\Omega} &= \frac{d^2U_{\parallel}}{d\omega d\Omega} + \frac{d^2U_{\perp}}{d\omega d\Omega} \\ &= \frac{1}{4\pi\varepsilon_0} \frac{e^2\omega^2}{4\pi^2 c} [|E_x|^2 + |E_y|^2] \end{aligned} \tag{2.17}$$

Assuming the slit aperture $h \to 0$ and in case of normal incidence, the result reduces to the Ginzburg-Frank formula (Eq. 2.2). The comparison between the TR and DR from a slit between two semi-planes angular spectra for a frequency of 1 THz and a slit aperture of $h = 5$ mm is shown in Fig. 2.8.

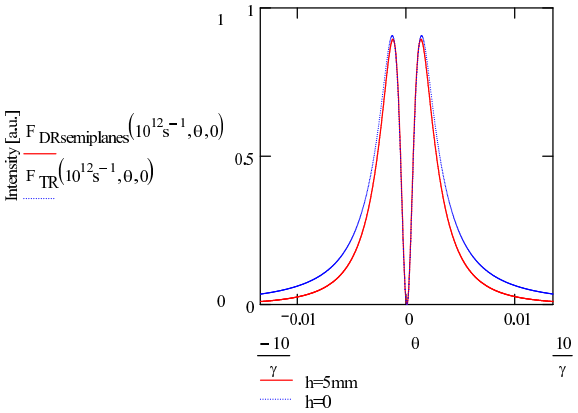

Figure 2.8: Comparison between the DR spectrum for different apertures, $h = 5$ mm and $h = 0$ (TR) at 1 THz.

2.1.3 Transition Radiation from a Finite Size Target

In this subsection we will discuss the importance of the size target in the modulation of TR power spectrum and show how far from the Ginzburg-Frank formula (Eq. 2.2) it is, being a complicate function of beam energy, target extension, frequency and angle of emission [15].

Since the extent of the particle field is of the order of $\lambda\gamma$, for high electron energy and large emitted wavelength, it may exceed the dimension of the radiation target, resulting in the spectrum to be frequency dependent, the

Ginzburg-Frank formula being not valid anymore. In practical cases, for $\gamma \approx 10^3$ and $\lambda \approx 1\ mm$, the target size should be much larger than 1 m and the finite size effect is always affecting measurements, resulting in a strong suppression of low-frequencies.

Following the approach already discussed in the previous section, the field generated by an electron at a distance R from the radiating target, which is assumed to be rectangular and of finite size, h, l being respectively the vertical and horizontal dimensions, is given by integrating Eq. 2.12 over the target surface, i.e. x from $-\frac{l}{2}$ to $\frac{l}{2}$ and y from $-\frac{h}{2}$ to $\frac{h}{2}$, so that

$$\begin{aligned} E_{x,y} \quad \propto \quad & \int_{-\frac{l}{2}}^{\frac{l}{2}} dx_s \int_{-\frac{h}{2}}^{\frac{h}{2}} dy_s e^{-i(k_x x_s + k_y y_s)} \\ & \int_{-\infty}^{\infty} d\kappa_x d\kappa_y \frac{\kappa_{x,y} e^{i(\kappa_x x_s + \kappa_y y_s)}}{\kappa_x^2 + \kappa_y^2 + \alpha^2} \end{aligned} \tag{2.18}$$

which becomes

$$\begin{aligned} E_{x,y} \quad \propto \quad & \int_{-\infty}^{\infty} d\kappa_x d\kappa_y \frac{\kappa_{x,y} e^{i(\kappa_x x_s + \kappa_y y_s)}}{\kappa_x^2 + \kappa_y^2 + \alpha^2} \\ & \frac{\sin[\frac{l}{2}(k_x - \kappa_x)]}{k_x - \kappa_x} \frac{\sin[\frac{h}{2}(k_y - \kappa_y)]}{k_y - \kappa_y} \end{aligned} \tag{2.19}$$

The integral over κ_x and κ_y can be evaluated by applying the integration methods of the analytic functions along proper close paths. The first integral is solved integrating the function

$$f(z) = \frac{z e^{i\frac{l}{2}(k_x - z)}}{(z^2 + f_y^2)(k_x - z)} \tag{2.20}$$

along the integration path shown in Fig. 2.9, being the contribution of the semi-circles to the integral negligible in the limit $r_1 \to \infty$ and $r_2 \to 0$. $z = \kappa_x + i\zeta$ and $f_y^2 = \kappa_y^2 + \alpha^2$.

The integral over κ_y is partially solved following the same procedure, the rectangular geometry allowing not to express the transition field in terms of elementary functions of k_x and k_y. The final expression for TR fields for horizontal and vertical polarization components from a finite size rectangular

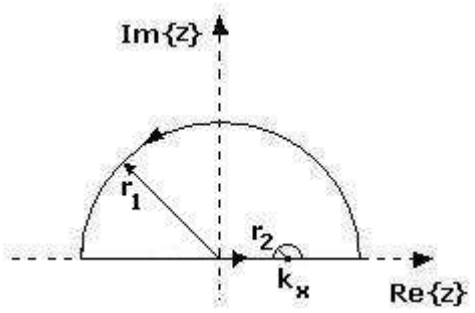

Figure 2.9: Contour along which the integral over κ_x is evaluated.

target are then given by [12]

$$
\begin{aligned}
E_x(k_x,k_y) &= \frac{ek}{2\pi^2 vR}\frac{(2\pi)^2 k_x}{k_x^2+k_y^2+\alpha^2} \qquad (2.21)\\
&\quad \Big\{\Big[1+\frac{e^{-\frac{h}{2}\sqrt{k_x^2+\alpha^2}}}{\sqrt{k_x^2+\alpha^2}}(k_y\sin(\frac{h}{2}k_y)-\sqrt{k_x^2+\alpha^2}\cos(\frac{h}{2}k_y))\Big]+\\
&- 4\pi\int_{-\infty}^{\infty}d\kappa_y\frac{\sin[\frac{h}{2}(k_y-\kappa_y)]}{k_y-\kappa_y}\frac{e^{-\frac{l}{2}\sqrt{\kappa_y^2+\alpha^2}}(k_x\cos(\frac{l}{2}k_x)+\sqrt{\kappa_y^2+\alpha^2}\sin(\frac{l}{2}k_x))}{\kappa_y^2+k_x^2+\alpha^2}\Big\}\\
E_y(k_x,k_y) &= \frac{ek}{2\pi^2 vR}\frac{(2\pi)^2 k_y}{k_x^2+k_y^2+\alpha^2}\\
&\quad \Big\{\Big[1+\frac{e^{-\frac{l}{2}\sqrt{k_y^2+\alpha^2}}}{\sqrt{k_y^2+\alpha^2}}(k_x\sin(\frac{l}{2}k_x)-\sqrt{k_y^2+\alpha^2}\cos(\frac{l}{2}k_x))\Big]+\\
&- 4\pi\int_{-\infty}^{\infty}d\kappa_y\frac{\sin[\frac{l}{2}(k_x-\kappa_y)]}{k_x-\kappa_y}\frac{e^{-\frac{h}{2}\sqrt{\kappa_y^2+\alpha^2}}(k_y\cos(\frac{h}{2}k_y)+\sqrt{\kappa_y^2+\alpha^2}\sin(\frac{h}{2}k_y))}{\kappa_y^2+k_y^2+\alpha^2}\Big\}
\end{aligned}
$$

The finite dimensions of the target produce a severe shift of the peaks, the greater the more the condition $\gamma\lambda$ much greater than the target size is far from being verified as shown in Fig. 2.10. In the limit $h, l \gg \frac{\gamma\lambda}{2\pi}$ the target can be considered of infinite extent and the angular distribution is well described by the Ginzburg-Frank formula.

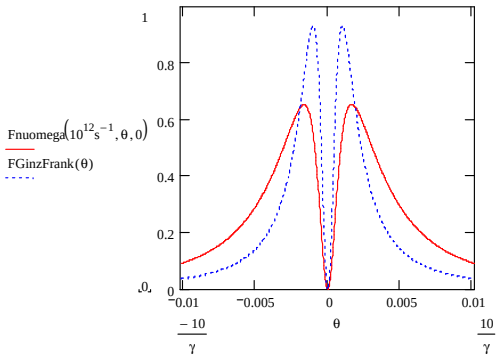

Figure 2.10: Comparison between the TR spectrum according to the Ginzburg-Frank formula and with correction due to the finite size target at 1 THz.

2.1.4 Diffraction Radiation from a Rectangular Hole in a Rectangular Target

This subsection concerns the derivation of the expression for DR spectrum from a rectangular aperture in a finite rectangular target, keeping in mind the result from the previous subsection and applying the Babinet principle.

In case of DR both low and high frequencies suppression may be observed at the same time due to the slit aperture, resulting in a more difficult reconstruction of the bunch profile.

Let assume the electron goes through the middle of the rectangular aperture with velocity $\vec{v}$ directed along the z-axis. The DR field from a rectangular hole, whose dimensions are (l, d), in a rectangular target can then be expressed, according to the Babinet's principle, as the difference between the TR fields for a target of vertical dimension equals to $2h + d$ and for a target of vertical dimension d so that

$$E^{DR}_{x,y}(k_x, k_y) = E^{TR}_{x,y}(k_x, k_y; l, 2h + d) - E^{TR}_{x,y}(k_x, k_y; l, d) \tag{2.22}$$

which becomes

$$\begin{aligned} E^{DR}_{x,y}(k_x, k_y) &= 4\frac{ek}{2\pi^2 vR}\int_{-\infty}^{\infty} \frac{d\kappa_x d\kappa_y \kappa_{x,y}}{\kappa_x^2 + \kappa_y^2 + \alpha^2} \frac{\sin[\frac{l}{2}(k_x - \kappa_x)]}{k_x - \kappa_x} \\ &\left\{ \frac{\sin[(h + \frac{d}{2})(k_y - \kappa_y)]}{k_y - \kappa_y} - \frac{\sin[\frac{d}{2}(k_y - \kappa_y)]}{k_y - \kappa_y} \right\} \end{aligned} \tag{2.23}$$

2.2 Coherent Radiation Theory

When a bunch of electrons moves in proximity of an edge, each electron in turn emits radiation, the effect of this "collective" emission on the diffraction radiation spectrum depends on the bunch longitudinal dimension.

Consider an electron bunch whose center of mass is the origin of a coordinate system (Fig. 2.11).

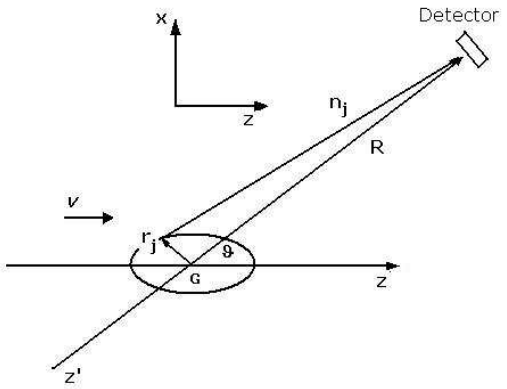

Figure 2.11: Schematic view of the bunch emission geometry.

Let us assume R as the distance from the source to the detector and $\hat{n}_j$ the unit vector which selects the observation direction for the jth particle, $\vec{r}$ being the position vector of the jth electron relative to its bunch center. Let $E_j = \exp\left(i\frac{2\pi}{\lambda}(ct - \hat{n}\cdot\vec{r}_j)\right)$ be the electric field generated by the jth electron.

In the assumption that the distance from the source to the detector is much larger than the extent of the bunch, $R >> \sigma_z$, the total field is given by the sum of the fields of each of the N particles and the total intensity can be written, in the limit of the Fraunhofer scalar theory, as

$$I_{tot}(\omega) = I_{sp}(\omega)\sum_{j,k} E_j E_k^* \tag{2.24}$$

with $I_{sp}(\omega)$ the intensity of radiation emitted by a single electron at frequency ω, where the sum over the two indexes can be expressed in terms of a sum of two terms as described in Eq. 2.25

$$I_{tot}(\omega) = I_{sp}(\omega)\Big(N + \sum_{j\neq k}^{N} \exp\left(i\frac{\omega}{c}\hat{n}\cdot(\vec{r}_j - \vec{r}_k)\right)\Big) \tag{2.25}$$

By averaging the expression in parenthesis over the positions of all the particles distributed along the bunch, the sum can be replaced by an integral

$$I_{tot}(\omega) = I_{sp}(\omega)\Big[N + N(N-1)\int\int drdr' C_2(\vec{r},\vec{r}' e^{i\frac{\omega}{c}\hat{n}\cdot(\vec{r}-\vec{r}')})\Big] \qquad (2.26)$$

where C_2 is the two particles distribution function normalized such that

$$\int\int drdr' C_2(\vec{r},\vec{r}') = 1 \qquad (2.27)$$

In the assumption the two particles are not correlated, the two particle distribution function can be written as $C_2(\vec{r},\vec{r}') \approx S(\vec{r})S(\vec{r}')$, furthermore being $S(\vec{r})$ real $S(\vec{r}) = S^*(\vec{r})$, the sum in Eq. 2.25 becomes

$$\begin{aligned}\sum_{j\neq k}^{N} e^{i\frac{\omega}{c}\hat{n}\cdot(\vec{r}_j-\vec{r}_k)} &= N(N-1)\int\int drdr' C_2(\vec{r},\vec{r}')e^{i\frac{\omega}{c}\hat{n}\cdot(\vec{r}-\vec{r}')} \qquad (2.28)\\ &= N(N-1)\Big|\int_{3D} d\vec{r}S(\vec{r})e^{i\frac{\omega}{c}\hat{n}\cdot\vec{r}}\Big|^2\end{aligned}$$

with the distribution function normalized such that $\int_{-\infty}^{\infty} S(\vec{r})d\vec{r} = 1$. The total spectrum can then be written as

$$I_{tot}(\omega) = I_{sp}(\omega)[N + N(N-1)F(\omega)] \qquad (2.29)$$

where

$$F(\omega) = \Big|\int_{3D} d\vec{r}S(\vec{r})e^{i\frac{\omega}{c}\hat{n}\cdot\vec{r}}\Big|^2 \qquad (2.30)$$

is the electron bunch 3D form factor. Two terms contribute therefore to the total intensity (Eq. 2.29): the first one, proportional to the number of particles, N, is the total intensity if the particles radiate all incoherently, each behaving independently one from the other; the second one, proportional to N^2, is dominant for short bunches when the N particles can be treated as a single macro-particle and the phase relations between particles play a fundamental role, the emission of radiation is then coherent.

As already mentioned, the TR or DR emission occurs mainly in two directions, forward and backward, with a maximum intensity at an angle $\vartheta \approx \frac{1}{\gamma}$. At small observation angles, $\vartheta \sim 0$, $\hat{n} \parallel \vec{r}$, so that

$$F(\omega) = \Big|\int_{-\infty}^{\infty} dzS(z)e^{i\frac{\omega}{c}z}\Big|^2 \qquad (2.31)$$

where $S(z) = \int_{\Sigma_\perp} S(\vec{r})dxdy$ is the 1D longitudinal distribution function of particles in the bunch, integration is performed over slices of area $\Sigma_\perp$ perpendicular to the z-axis. It follows that a measurement of the coherent emission spectrum is a measurement of the form factor, providing information about the longitudinal bunch distribution. However, a measurement in this condition is not feasible since both TR and DR from a slit do not produce radiation at $\vartheta = 0$, an off-axis observation is then needed. The scalar product becomes then $\hat{n} \cdot \vec{r} = x \sin\vartheta + z \cos\vartheta$, depending on both observation angle and transverse dimensions. Because of an interference effect of radiation which is emitted from different positions in the cross section of the beam, both contribution will result in a measured bunch length longer than the real one. For example, for a cylindrical bunch with radius ρ and length σ_z, the form factor is

$$F(\omega) \propto \left| \frac{J_1(\frac{\omega\rho}{c}\sin\vartheta)}{\frac{\omega\rho}{c}\sin\vartheta} \frac{\sin(\frac{\omega\sigma_z}{2c}\cos\vartheta)}{\frac{\omega\sigma_z}{2c}\cos\vartheta} \right|^2 \tag{2.32}$$

where J_1 is the first order Bessel function. It follows that for $\vartheta = 0$, Eq. 2.32 gives the *sinc*-squared function typical for uniform-distributed electron bunches. For large angles and big transverse beam size, the bunch length will result longer than the real one. However, in the limit (assumed to be valid from now on) $2\pi\rho\tan\vartheta \ll \sigma_z$, corrections are not needed and the longitudinal bunch distribution can be retrieved by Fourier-inverse transforming Eq. 2.31 as follows

$$S(z) = \frac{1}{\pi c}\int_0^\infty d\omega \sqrt{F(\omega)} \cos\left(\frac{\omega z}{c}\right) \tag{2.33}$$

only the *cos*-term being involved since $S(z)$ is real. Eq. 2.33 does not allow to get information on the bunch asymmetry due to the fact that it is a cosine transform. Furthermore, even for a symmetric bunch, the result does not define a unique bunch profile, since the phase information is missing.

The next section will treat a method to get the maximal information about the bunch shape from the measured spectrum.

2.3 Kramers-Kronig Method

Even though the assumptions of non-negative and real electron distribution have been done, there are infinite distributions which give the same autocorrelation function, since its Fourier transform gives only the absolute magnitude, $|\sqrt{F(\omega)}|$, of the form factor. A method, based on Kramers-Kronig

dispersion relation and suggested by [19], has been used to retrieve the phase and eliminate the ambiguity in the reconstruction procedure. The method takes advantage of the analogy with the input-output response analysis used in optics. In this section an overview of the theory concerning the procedure is given.

2.3.1 Contribution to the Form Factor

Let us reconsider the integral which defines the complex form factor $F(\omega)$ as the product of an amplitude term $A(\omega)$ and a phase term $e^{i\psi(\omega)}$

$$S(\omega) = \int_0^\infty S(z) e^{i\frac{\omega}{c}z} dz \equiv A(\omega) e^{i\psi(\omega)} \tag{2.34}$$

so that

$$F(\omega) = S(\omega)S^*(\omega) = A^2(\omega) \tag{2.35}$$

$\omega = \omega_r + i\omega_i$ being complex.

To apply the Kramers-Kronig relation, the electron bunch distribution function has to fulfill these conditions:

1. $S(z) = 0 \; \forall \; z < 0$
2. $S(z)$ finite everywhere and $E(\omega) \to 0$ as $1/\omega$ for $|\omega| \to \infty$
3. $S(z)$ smooth and for $z \to \infty$ $S(z) \to z^{-2}$

The first condition expresses the causality principle, whose consequence is that the spectral function $A(\omega)$ is a square-integrable function which can be extended almost everywhere to give a function analytic in the upper half complex plane.

Recalling the expression for the total emitted intensity (Eq. 2.29), we can neglect the incoherent contribution with respect to the coherent part, which dominates in the FIR region for sub-picosecond bunches. Therefore, the total electric field emitted by a bunch of N electrons is linearly dependent on the electric field emitted by the single electron as

$$\vec{E}_{tot}(\omega) = \sqrt{N(N-1)} S(\omega) \vec{E}(\omega). \tag{2.36}$$

This describes a linear causal relation in analogy with the input-output response function analysis used in optics to obtain the complex reflectivity at an interface, where the integral in expression 2.34 is replaced by an integral

over positive time due to causality. Hence, the function $S(\omega)$ defined in Eq. 2.34 is analytic for all complex values of ω in the upper half of the complex plane and assuming it decays in a power law with $|\omega| \to \infty$ (condition 2.), the Kramers-Kronig relation connecting the modulus and the phase is then obtained introducing

$$\ln S(\omega) = \ln A(\omega) + i\psi(\omega) \tag{2.37}$$

being a convenient way to separate the Fourier spectrum into real and imaginary parts.

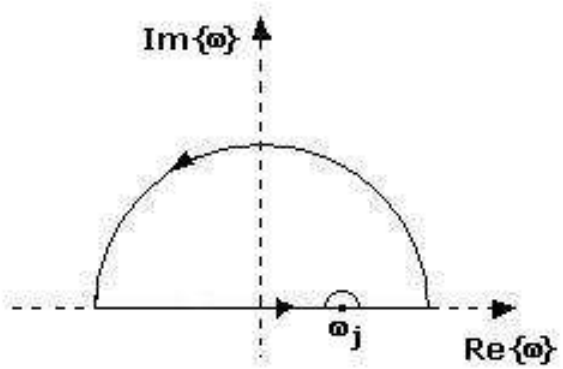

Figure 2.12: Path of integration for the Cauchy integral.

The dispersion relation of Eq. 2.37 is therefore

$$\psi_m(\omega) + \psi_{Blaschke}(\omega) = -\frac{2\omega}{\pi} P \int_0^\infty dx \frac{\ln \rho(x)}{x^2 - \omega^2} + \sum_j arg\Big(\frac{\omega - \omega_j}{\omega - \omega_j^*}\Big) \tag{2.38}$$

where ψ_m is the minimal phase, $\psi_{Blaschke}$ is the phase of the Blaschke product and ω_j^* are the zeros of $S(\omega)$ in the upper half of the complex frequency plane, P is the Cauchy principal value of the integral. $\psi_{Blaschke}(\omega)$ is zero if $S(\omega)$ does not have any zero in the upper half plane. Zeros on the real axis give no contribution to the phase.

The minimal phase evaluated from the first term of Eq. 2.38 is a good estimation of the real phase if the form factor has no nearby zeros in the upper half of the complex frequency plane. The minimal phase is then obtained from the Kramers-Kronig relation (Eq. 2.37). The singularity at $x = \omega$ can be removed by adding to Eq. 2.38 the term

$$-\frac{2\omega}{\pi} P \int_0^\infty dx \frac{\ln A(\omega)}{x^2 - \omega^2} = 0 \tag{2.39}$$

Finally, the minimal phase is calculated from

$$\psi_m(\omega) = -\frac{2\omega}{\pi}\int_0^\infty dx \frac{\ln[A(x)/A(\omega)]}{x^2-\omega^2} \tag{2.40}$$

Hence, from the measured form factor, $F(\omega)$, the amplitude term $A(\omega)$ can be determined (Eq. 2.35) and used to calculate the frequency dependent phase, $\psi_m(\omega)$, the complete dependence of the complex form factor on the frequency being therefore evaluated.

By inverse Fourier transforming Eq. 2.34, the bunch density distribution is obtained

$$S(z) = \frac{1}{\pi c}\int_0^\infty d\omega A(\omega)\cos\left[\psi_m(\omega) - \frac{\omega z}{c}\right] \tag{2.41}$$

depending only on the *cos*-term since $S(z)$ is real. The information about the asymmetry on the bunch density distribution is contained in the non-linear contribution to the frequency-dependent phase factor $\psi_m(\omega)$.

2.3.2 Asymptotic Limits

Once the spectrum is measured, the form factor, and then the asymmetric bunch shape, can be reconstructed entirely in both amplitude and phase. However, due to the strong suppression of the spectrum at both low and high frequencies, asymptotic forms for $F(\omega)$ are needed in both the low and high frequency region. Furthermore, at high frequencies the signal is covered by the background noise, a curve which describes how the form factor goes to zero in this range is then needed.

Since the bunch distribution, $S(z)$, is a real function, the modulus, $A(\omega)$, of the spectral function is an even function of ω. Expanding Eq. 2.34 in a power series of ω gives

$$S(\omega) = \sum_{n=0}^{\infty}\frac{i^n}{n!}\left(\frac{\omega}{c}\right)^n < z^n > \tag{2.42}$$

where $< z^n >= \int_0^{\sigma_z} z^n S(z)dz$ is the nth moment of the distribution function, the integral extending over a finite region due to the finite size, σ_z, of the bunch. The low-frequency asymptote for the form factor is then found to be a parabolic function

$$F(\omega) \to 1 - c\omega^2 \quad for \quad \omega \to 0 \tag{2.43}$$

c being a positive factor.

The high frequency asymptote is a more complicate issue since it depends on the behavior of the bunch distribution, $S(z)$, near the end points, which are assumed to be at $z = 0$ and $z = \sigma_z$ so that $S(0) = S(\sigma_z) = 0$. Integrating by parts Eq. 2.34, we obtain

$$S(\omega) \simeq \frac{e^{i\frac{\omega}{c}z}S(z)}{i\frac{\omega}{c}}\Big|_0^{\sigma_z} - \frac{e^{i\frac{\omega}{c}z}S'(z)}{(i\frac{\omega}{c})^2}\Big|_0^{\sigma_{\sigma_z}} + ... \tag{2.44}$$

the first term being zero because of the boundary conditions, the main contribution coming from the term proportional to ω^{-2}. Hence at high frequencies the form factor varies as ω^{-4}.

Chapter 3

Experimental Setup

In the present chapter, an overview of the main linac components involved in the measurement and a description of the experimental setup, i.e. diffraction radiator, interferometer and detectors, is given. Results from the Golay cell detector calibration are discussed, details can be found in Appendix C.

3.1 Injector and Bunch Compressors

The standard FEL operation of the TTF linac at 1 GeV electron energy requires a peak current of 2.5 kA to produce radiation wavelength of 6 nm.

The RF gun, commissioned and characterized at PITZ (DESY Zeuthen) [23], is a 1.5 cell L-band cavity, resonating at a frequency of 1.3 GHz and powered by a 5 MW klystron. A high quantum efficiency Cesium Tellurite (Cs_2Te) photocathode [21], illuminated by a laser with wavelength of 262 nm, delivers electron bunches with charges up to 4 nC, depending on the laser energy. A solenoid magnet, placed around the RF gun, focuses the electron beam in order to reduce space charge induced emittance growth [24].

Starting from 5 MeV electron energy and 2.2 mm rms bunch length at the gun exit, the beam is accelerated to 127 MeV and compressed longitudinally in a standard four bend magnetic chicane (BC2) as shown in Fig. 3.2. The compression is obtained by changing the accelerating module phase such that the electron bunch is accelerated on the rising slope of the RF electric field (off-crest acceleration) (Fig. 3.1b), resulting in a different energy distribution of the electrons in the bunch: on the head particles with lower energy than

the nominal one and on the tail particles with higher energy. This momentum kick can be described in the linear approximation by

$$\Delta E = E_{cav} \cos\left(\frac{2\pi z}{\lambda_{RF}} + \phi\right) \tag{3.1}$$

where λ_{RF} is the RF wavelength, E_{cav} the maximum energy achievable if the beam is injected into the linac on-crest[1] and ϕ the off-crest phase.

The bunch enters then the magnetic chicane where higher energy electrons follow a shorter trajectory than those with lower energy. The difference path length gives lower energy particles a chance to catch up for efficient compression, as shown in the sketch of a bunch compressor (Fig. 3.1a).

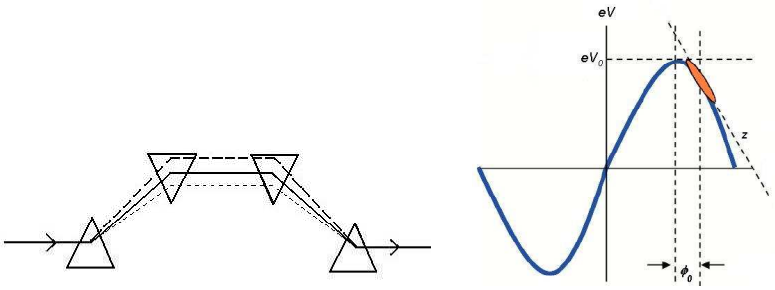

(a) Sketch of a magnetic chicane (b) Off-crest acceleration

Figure 3.1: Sketch of the compression mechanism.

Two additional accelerating modules (ACC2 and ACC3), placed before a second bunch compressor (BC3), accelerate the beam further to 380 MeV. BC3 is a 4-bend S-chicane compressor, designed [25] to minimize coherent synchrotron radiation (CSR) effects, which can induce dramatic emittance growth [22].

The two-stage compression is necessary to avoid space charge induced emittance dilution and to reduce non-linear effects due to RF fields. The compressor parameters design values are listed in table 3.1 and a sketch of the two-stage bunch compression system is given in Fig. 3.2.

Even though starting with long bunches allows to consider negligible space charge forces which would be indeed very strong because of the low initial energy, it produces however a large RF induced correlation in the energy-phase plane after acceleration. Because of the very small uncorrelated energy spread from the RF gun, the effect of the RF curvature results after

[1]The on-crest operation corresponds to the phase point of lowest emittance and beam energy spread; the electron bunch is accelerated on the peak of the electric field.

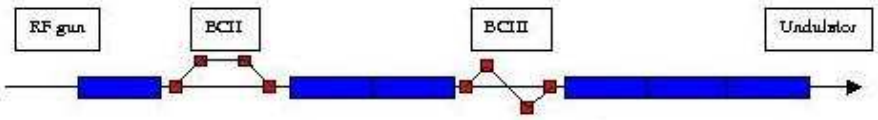

Figure 3.2: Sketch of the two-stage compression at the VUV-FEL.

Compressor Parameters	**BC2**	**BC3**
Type	Standard	S-chicane
Angles $[deg]$	17.5	3.8
R_{56} $[mm]$	-170	-49
T_{566} $[mm]$	276	75
E $[MeV]$	130	440
Final I $[A]$	320	2500

Table 3.1: Two-stage compressors' design parameters

compression in a sharp peak with a long tail in the longitudinal profile. The major contribution to the FEL process comes from the spike which carries the required peak current for lasing. In chapter 4 it is shown the agreement between the simulated bunch profile and the one obtained from experimental results.

To remove this curvature a superconducting 3^{rd} harmonic cavity is planned to be installed before the first compressor.

3.2 Diffraction Radiation Target

The diffraction radiation target is placed at 45^o with respect to the direction of propagation of the beam, downstream from bunch compressor BC3, in the vacuum pipe. It is made of two, 300 nm thick, 46 x 20 mm wide, silicon foils coated on the beam facing side with 40 nm aluminum, in a frame driven by a stepper motor[2], which allows highly precise movements. The two foils

Figure 3.3: Diffraction radiation target.

(see fig. 3.3) are the jaws of a slit. The slit can be brought into position in the vacuum chamber with a resolution of 5 $\mu m/step$. One of the jaws can then be moved with respect to the other in the 0 to 10 mm range, with a resolution of 2.5 $\mu m/step$. End-stop safety switches limit the movable jaw travel.

Everything is computer controlled via DOOCS [26], the DESY accelerator control system.

[2]MAE - `www.pennmotion.com`

3.3 Experimental Apparatus

Radiation coming from the diffraction radiation target goes through a crystalline quartz window (z-cut, clear aperture of 60 mm, 4.8 mm thick) (fig. 3.5) and impinges on a parabolic mirror, whose focal point is in the target plane. The sketch of the experimental apparatus up to the interferometer entrance is shown in figure 3.4. The mirror produces a parallel beam which is

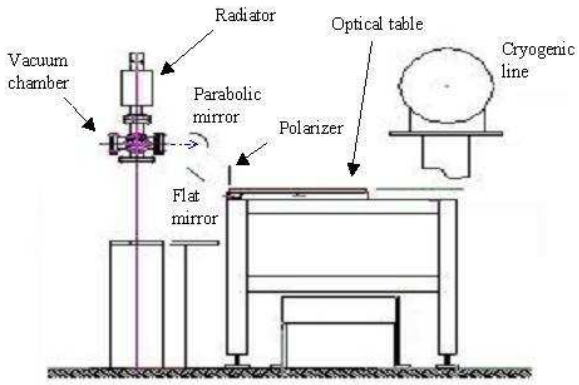

Figure 3.4: Sketch of the experimental apparatus.

reflected vertically down towards an aluminum flat mirror, placed at 45^o with respect to the horizontal plane, which reflects radiation horizontally into the interferometer.

The crystalline quartz window is transparent to millimeter and sub-millimeter wavelengths allowing an almost flat 80% transmission, except for a sharp absorption peak at 78 μm, and it is compatible with ultra-high vacuum (UHV) atmosphere [28]. In Fig. 3.5 the plot shows the transmission of crystalline quartz for ordinary rays. In appendix B, the most suitable materials for millimeter and sub-millimeter applications are reported.

Both the flat and the parabolic mirrors have polished aluminum surfaces, whose roughness is less than 1/10 of the wavelength, resulting in a very good reflectivity and negligible absorption losses. The parabolic mirrors mounted on the experimental apparatus are 90^o off-axis[3] mirrors whose effective focal length (200 mm) is twice the focal length of the full paraboloid. All the electromagnetic waves with frequency lower than the plasma frequency of the metal, for Al $\omega_p = 3.5510^{15}\ Hz$ [27], are almost totally reflected at the metal

[3]The optical and mechanical axis do not coincide, resulting in a reduction of losses and chromatic aberrations.

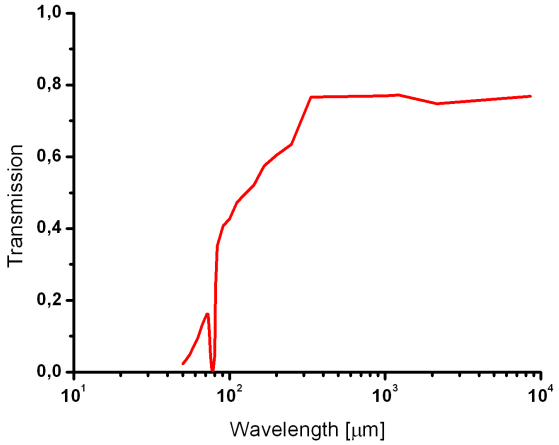

Figure 3.5: Transmission curve for ordinary rays of crystalline quartz.

surface. Moreover, the parabolic mirror minimizes chromatic aberrations for a point-like source.

3.3.1 Martin-Puplett Interferometer

The interferometer is a Martin-Puplett type [29], the polarizing version of the Michelson one, where the Michelson beam splitter is replaced by a polarizer which splits the polarizations and plane mirrors by roof mirrors. A simplified sketch of a Martin-Puplett interferometer is shown in Fig. 3.6. A theoretical treatment is given in appendix D.

The radiation, coming from the plane mirror, enters the first polarizer (P) whose wires, in our case, are horizontal to let vertical polarization through. The vertically polarized transmitted radiation first reaches the beam splitter (BS), placed at 45^o, whose wires are at 45^o to the horizontal plane when viewed along the beam input axis. The BS splits the input signal into two equal, orthogonally polarized components, one being reflected towards the stationary roof mirror and the other being transmitted to the moveable one, whose maximum travel distance is 50 mm with a minimum step width of 2.5 μm. Radiation coming back from both arms to the beam splitter recombines and is focused onto the Golay cell detectors by a second parabolic mirror via the analyzing grid (A), located between the mirror and the detectors, which transmits the component orthogonal to the wires to detector number 1 and reflects the component parallel to the wires to detector number 2.

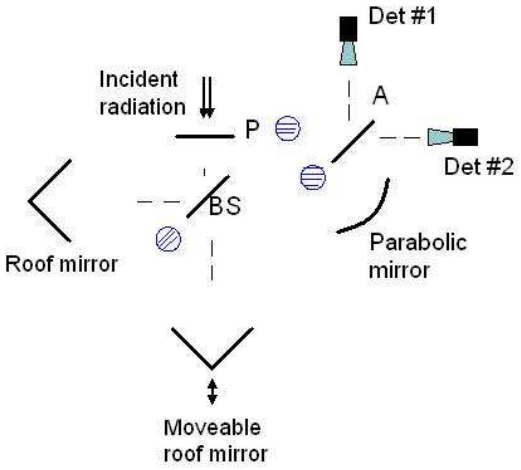

Figure 3.6: Sketch of a Martin-Puplett interferometer.

A quantitative approach to Fourier transform spectroscopy is given in appendix D.

Polarizers

At millimeter wavelengths, polarizers can be built as planar system of metallic wires equally spaced. Any electric field incident on such a system can be considered as composed of two orthogonally polarized components, one with its electric vector parallel to the wires and the other orthogonal to them.

The field parallel to the wires induces a current along each wire, whose resulting distribution is equivalent to the one induced on the surface of a metallic flat mirror. The parallel component of the electric field is therefore reflected, while the orthogonal component, which does not induce any significant amount of current along them, is almost completely transmitted.

For an ideal beam splitter, the reflectivity and transmittivity coefficients does not depend on the frequency and no absorption losses occur so that

$$|r|^2 + |t|^2 = 1 \tag{3.2}$$

In the case of real beam splitter, the reflectivity and transmittivity will depend on the wavelength and the dependence is known. If the wire diameter d and the spacing s between wires are small compared to the wavelength of the incident radiation, the grid power reflectivity for the parallel and normal

electric field components is given by Eq. 3.3 [30],

$$\begin{aligned} |r_p|^2 &= \left[1 + \left(\frac{2s}{\lambda} \ln \frac{s}{\pi d}\right)^2\right]^{-1} \\ |r_n|^2 &= \frac{\pi^4 d^4}{(2\lambda s)^2 [1 + \frac{\pi^4 d^4}{(2\lambda s)^2}]} \end{aligned} \tag{3.3}$$

The 90 mm wire grids are wound from 10 μm diameter gold-plated Tungsten wire with 30 μm spacing.

Even though reflectivity is wavelength dependent, it is straightforward to verify, as shown in Fig. 3.7 that such beam splitters can be considered almost ideal over a wide millimeter wavelength range.

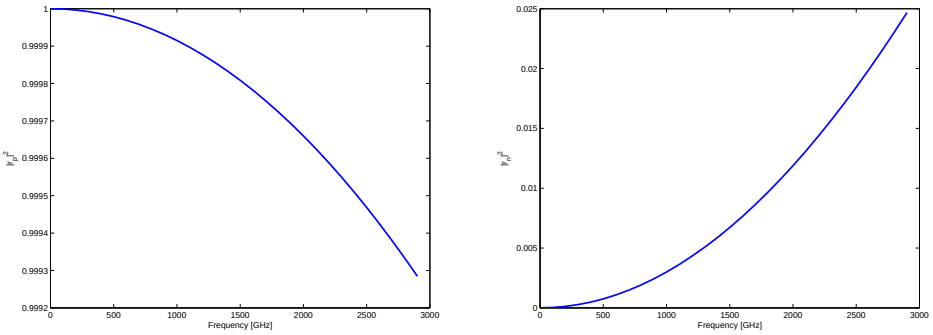

(a) $|r_p|^2$ (b) $|r_n|^2$

Figure 3.7: Transmission and reflection components of the beam splitter.

Roof Mirrors

A roof mirror consist of two plane metal reflectors in contact along one edge, which defines the roof line, at an angle of 90^o. A sketch of a roof mirror is shown in Fig. 3.8. It has the property of altering the polarization state of an incident field upon reflection as illustrated in the figure.

A plane normally polarized radiation, with its electric vector aligned at an angle θ to the roof line, impacts one of the mirror surfaces. After reflection from both surfaces the outgoing radiation plane of polarization is rotated through an angle 2θ, so that the electric vector angle to the roof line is now $-\theta$. Since the BS wires are oriented at 45^o with respect to the vertical plane, a 45^o input polarization parallel to the wires is reflected towards the roof

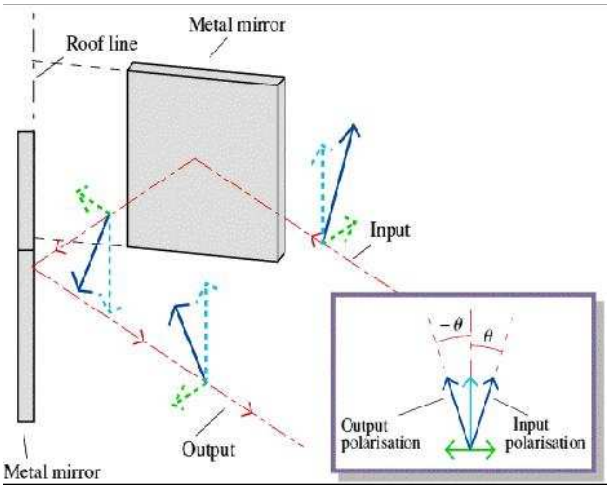

Figure 3.8: Sketch of roof mirrors working principle

mirror and reflected back to the BS so that the $\vec{E}$ field component is now orthogonal to the BS wires[4].

3.3.2 Comparison with a Michelson Interferometer

Compared to a Michelson interferometer, the Martin-Puplett has the advantage of an almost perfect beam splitter, since the reflectivity and transmittivity coefficients depend on wires geometric factors and not on the material used. Suitable intensity beam splitter for the far infrared radiation do not provide indeed equal reflectance and transmittance for all frequencies and interference effects due to the thickness of the splitter may occur, resulting in a reflected/transmitted intensity which is a complicate function of frequency.

Furthermore, on average half the power from the source is reflected back to it with a Michelson device while, in principle, no intensity is lost in a Martin-Puplett interferometer, being the initial intensity equal to the sum of the intensities from both detectors.

Finally, the difference signal can be normalized to the sum of the signals from both detectors, one detecting the horizontal polarization, $V_h(x)$, while the other the vertical one, $V_v(x)$, yielding an interference pattern, $\delta(x)$, which is independent on current density fluctuations in the electron beam as stated

[4]Wire grids and mirrors are provided by DESY.

by Eq. 3.4

$$\delta(x) = \frac{V_h(x) - V_v(x)}{V_h(x) + V_v(x)} \tag{3.4}$$

3.3.3 Simulations

Two codes, ZEMAX[5] and THz Transport[6], might be used to provide a first understanding of the interferometer response.

In the previous chapter, we focused our attention on the contribution of the coherent part of the radiation spectrum, $I_{tot}(\omega)$, to the longitudinal bunch size through the bunch form factor, $f(\omega)$, as stated in equation 3.5

$$I_{tot}(\omega) = I_{sp}(\omega)[N + N(N-1)|f(\omega)|^2] \tag{3.5}$$

N being the number of electrons per bunch and $I_{sp}(\omega)$ the single-particle spectrum. The measured spectrum, $I_{meas}(\omega)$, is then proportional to $I_{tot}(\omega)$ through the transfer function $T(\omega)$ which depends on windows, grids, mirrors, detectors. $T(\omega)$ can be obtained either through calibration with a known source (as done for the detector transfer function) or calculating it with the above codes.

Both codes use scalar Fresnel diffraction theory. The THz Transport has been here preferred because it is freeware and much more user-friendly. However, studies [31] show the consistency of results from both codes.

THz Program

THz Transport is a Mathematica code which calculates the source function on grids, free propagates the radiation through each component up to the last surface, in the present case given by the detector window, and calculates the output intensity.

It uses the approximation of circular target. The approximation plays a crucial role mostly at low frequencies where the transverse extension of the field, being of the order of $\gamma\lambda$, is comparable to the target size.

Figure 3.9 shows the transfer function of the Martin-Puplett interferometer for a diffraction radiation source with 5 mm slit aperture and 380 MeV electron beam energy.

The simulations have a 10% error due to the uncertainty in the numerical integration.

[5]Commercially available (`www.zemax.com`).

[6]Written by Bernhard Schmidt (`www.desy.de/schmidtb/THzTransport`).

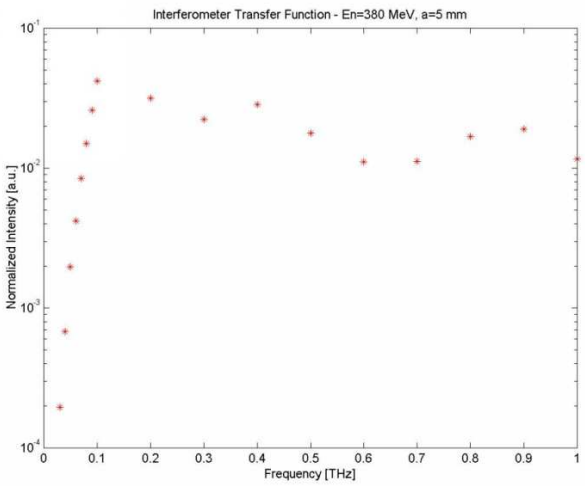

Figure 3.9: VUV-FEL interferometer transfer function simulated with THz-Transport Code. Wire grids are treated as apertures. $E_{ebeam} = 380\ MeV$, slit aperture 5 mm.

3.3.4 Alignment of the Interferometer

Before installing the interferometer in the tunnel, a first and accurate alignment has been done in the THz Laboratory at DESY.

Mylar foils have been mounted both on the beam splitter and on the analyzer, paying attention to keep the same plane of the wires. This procedure has been useful to align the interferometer components with respect to each other and fix their positions on the optical table. In this way the Martin-Puplett interferometer is used as a Michelson one.

A 5 mW *He-Ne* laser has been used both with an expander to make a parallel beam with a 30 mm diameter spot and without it to perfectly align the roof mirrors. The laser was sent through a pinhole, to stop back scattered radiation onto the moveable roof mirror and aligned in such a way that the spot is exactly on the roof line. A "round trip" ensured that incoming and reflected beam were superimposed. Both the roof and the parabolic mirrors are equipped with micrometric screws to finely adjust position and angle.

In the tunnel the interferometer is mounted on a purposely designed and built alignment table, providing vertical and horizontal tilt. The entire system was aligned with respect to the beamline and to the ground first with an alignment laser propagating through the beampipe with the diffraction radiator inserted and closed, then with a *He-Ne* laser placed on the vacuum

window opposite the z-cut quartz window and the radiator extracted.

3.4 Detectors

In this section a brief introduction on the thermal detector characteristics is reported, paying more attention on two detectors usually used to detect far-infrared radiation, the Golay cell and the pyroelectric detectors, the former being chosen for our measurements for reasons discussed in the next paragraph.

One of the main issues in the characterization of the electron bunch longitudinal density profile is the reconstruction of its shape affected by the low frequency cut-off due to the vacuum pipe, the interferometer components and the detector acceptance. For this reason knowledge of the frequency response of the detector, in particular in the millimeter and sub-millimeter range [35], is essential in order to correct the results and extrapolate a bunch shape as close as possible to the real one.

Thermal detectors respond to temperature rise due to the absorption of radiant energy. The main parameter is the detector sensitivity or Noise Equivalent Power (NEP), which is the rms value of the incident chopped power necessary to produce a Signal-to-Noise ratio of 1. Since the rms electrical noise is calculated per unit square root bandwidth, the units for NEP are $\frac{W}{\sqrt{Hz}}$.

3.4.1 Golay Cell Detector

Golay cells were developed during World War II by M.J.E. Golay in order to detect aircraft by measuring their radiated heat. Their development came to an end when radars became available [33].

A Golay cell detector is a thermo-acoustic detector consisting of a small cell filled with a gas, typically Xenon because of its low thermal conductivity, and a sensitive heat absorbing film[7] with low thermal capacity which ensures a flat response to different frequencies. The frequency dependence is given, in principle, only by the properties of the window material used.

Figure 3.10 shows a sketch of the inner components of the Golay cell detector and the optics system associated with it.

[7]In our case, it is produced by aluminizing an extra-thin (0.2 μm thickness) cellulose layer.

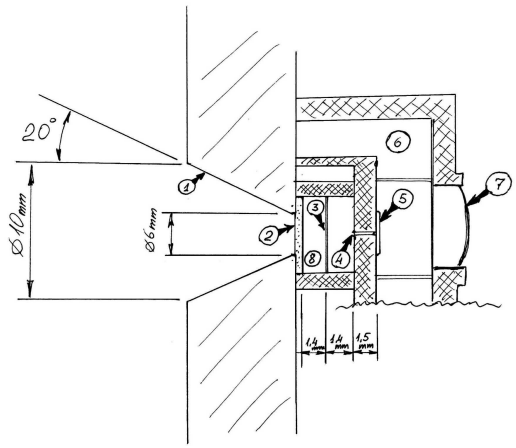

(a) The Golay cell

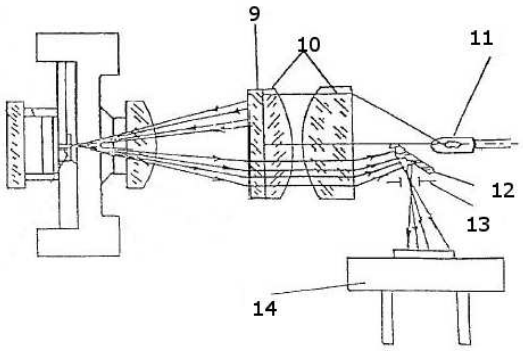

(b) The optics system

Figure 3.10: Sketch of a Golay cell detector. 1. Polished metal input cone to increase the radiation angular acceptance; 2. Input window; 3. Absorbing film; 4. Signal and compensation channel; 5. Sensitive mirror membrane; 6. Vacuum chamber; 7. Objective; 8. Gas chamber; 9. Grid; 10. Double-lens system; 11. LED; 12. Mirror; 13. Grid; 14. Photocell.

Radiation, mostly in the IR region, goes through the window and is absorbed by the film warming it and the contained gas up. The gas therefore expands and the resulting pressure change modifies the shape of the flexible aluminized membrane (5) at the back of the cell, which acts as a mirror. In order to compensate for changes in room temperature there is a small "leak" to a reservoir from the gas cell (4). To convert the membrane movement into an electrical signal, a light emitting diode (LED) (11) illuminates, through a double-lens system (10), the back of the flexible mirror. A grid (9) and a lens are placed in front of the flexible mirror in such a position that, in absence of any movement of the mirror, an image of one part of the grid is superimposed on another part of the grid. The reflected light then repasses through the double-lens system and is focused onto a photocell (14).

In principle, due to the thin absorbing film in the cell, the optical response is flat over a wide spectral range (from 1 μm up to several mm), the limiting feature being the window aperture and the material chosen. In our case, the diamond window mounted on the detector is transparent for almost all wavelengths, but the flatness behavior has to be verified (details in next section and in Appendix C).

The Golay cells used in the experiment are type OAD-7 (Optical Acoustic Device) from QMC[8] Instruments; their characteristics are listed in table 3.2. Because of its high sensitivity and wide bandwidth in the millimeter range,

Window Material	Diamond
Free Aperture Diameter	6 mm
Mechanical Diameter	8 mm
Window Thickness	0.4 to 0.5 mm
Wedging	no (plane/plane faces)
Response BW	$0 - 35$ Hz
NEP @ 20 Hz	$10^{-10} \frac{W}{\sqrt{Hz}}$

Table 3.2: Golay cell detector characteristics

the Golay cell detector has been preferred to a pyroelectric one. In terms of the Noise Equivalent Power or NEP it is of the order of 10^{-10} $\frac{W}{\sqrt{Hz}}$. The

[8] `www.terahertz.co.uk`

main drawback is the slow temporal response (decay time of the order of tens of ms), the limit to the speed of detection being determined by the relative values of the thermal capacity and thermal conductivity. However in the present case it is not a critical issue since the highest macropulse repetition rate is 5 Hz. To obtain the best performance from a Golay cell detector, it is recommended to shield it from abrupt temperature variations and to limit the amount of power which may destroy the membrane. The removal of any kind of vibrations is also advisable, in particular vacuum pumps might cause problems.

A first check of the Golay cell characteristic has been done in the laboratory by using a blackbody radiation source. The detector response was checked at the TTF working frequency, 2 Hz or 5 Hz (Fig. 3.11).

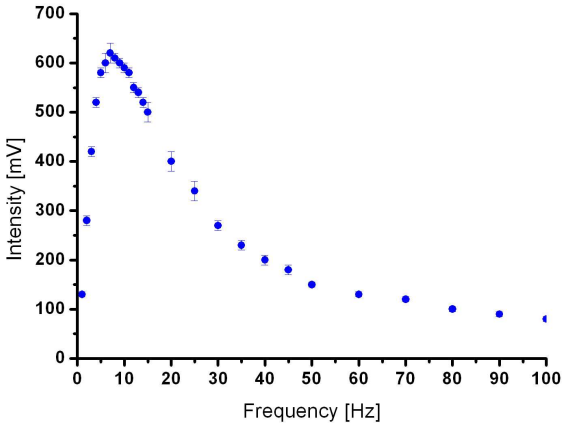

Figure 3.11: Golay cell detector response as function of the chopping frequency.

Even though the maximum signal is detected at 7 Hz, the best chopping frequency value, for which the NEP has a minimum, is found to be 20 Hz.

Before starting the measurement, the detector has been tested at TOSY-LAB[9] with a synchrotron radiation source. Results are shown in Fig. 3.12.

The oscilloscope has been set in AC coupling with an output impedance of 1 $M\Omega$, since in DC coupling a large offset (roughly -10 V) is shown for measurement at high impedance.

In these measurements we could not operate at low impedance (50 Ω) because the internal circuit of the detector is such that it cannot feed device

[9]**T**erahertz and **O**ptical **Sy**nchrotron Radiation **Lab**oratory - DESY Hamburg.

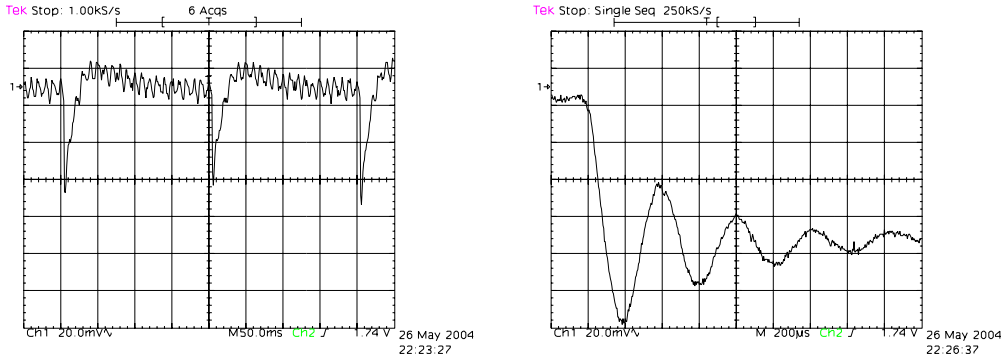

(a) 50 ms/div (b) 200 $\mu s/div$

Figure 3.12: Signal from the Golay cell detector with synchrotron radiation source.

with impedance lower than 2 $k\Omega$. This is also the reason why we could not see the signal on the ADC, since its input impedance is 1 $k\Omega$.

For further measurements, a circuit to adapt impedance and let the signal be directly read by a fast ADC has been designed and built.

Fig. 3.12b, which shows details of the pulses in figure 3.12a, shows damped oscillations around the peak with period of roughly 400 μs believed to be due to vibrations of the cell absorbing film when a signal is incident on it, giving rise to a resonance effect.

3.4.2 Pyroelectric Detector

Pyroelectric detectors, being thermal detectors, produce a signal in response to a change in their temperature. Below a temperature T_c, known as Curie point, ferroelectric materials (Triglycine sulfate, Lithium, Tantalate) exhibit a large spontaneous electrical polarization. If the temperature is altered by an incident radiation, the polarization changes and, if electrodes are placed on opposite faces of a thin dielectric, forming a capacitor (Fig. 3.13), the change in polarization can be observed as an electrical signal.

The process is independent on the wavelength of the incident radiation, resulting in a flat response over a wide spectral range. The limiting feature is either the sensor size or the window material used in the manufacture of its housing. By using a suitable material it is possible to detect radiation of different frequencies up to 1 mm. The main advantage is the fast temporal

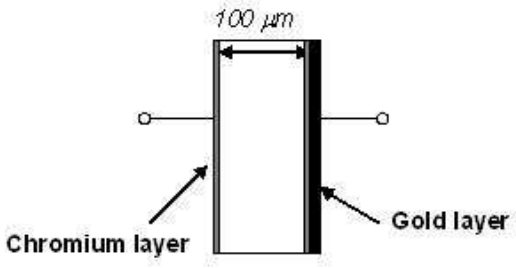

Figure 3.13: Sketch of the pyroelectric detector.

response, being the faster the lower is the resistance, a feature which is evident in the test at TOSYLAB with synchrotron radiation (same conditions of Golay cell operation) and depicted in Fig. 3.14.

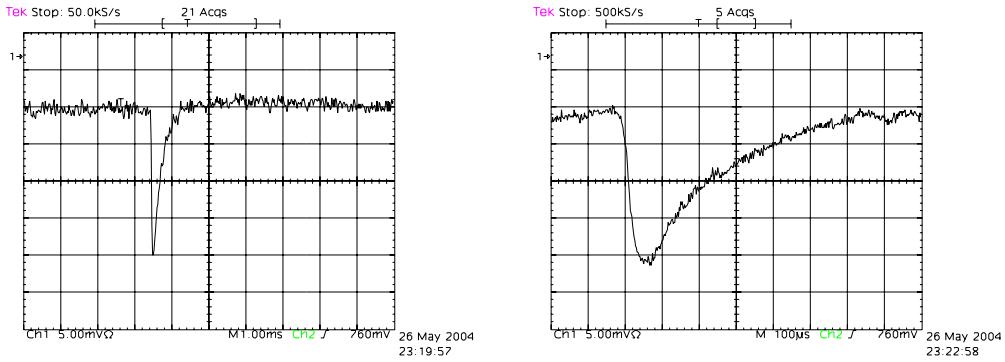

(a) 1 ms/div (b) 100 $\mu s/div$

Figure 3.14: Signal from the Molectron P1-45 pyroelectric detector with synchrotron radiation source at TOSYLAB.

Thanks to the fast temporal response, pyro-detectors are used as bunch compressor monitors both at DBC2 and DBC3 to give a rough estimation for the maximum compression.

3.5 Golay Cell Calibration

The calibration has been performed using three different technique depending on the explored spectral regions:

- Millimeter wave generator in the 75 - 110 GHz (equivalent to 4 - 2.7 mm) bandwidth
- Hot-Cold method for four selected wavelengths: 2.1 mm, 1.4 mm, 1.1 mm, 850 μm
- FEL radiation source in the range 100 - 160 μm

the goal being the definition of the detector responsivity as

$$R[V/W] = \frac{Measured\ Voltage\ Response}{Incident\ Power} \tag{3.6}$$

as function of the frequency.

3.5.1 Millimeter Wave Generator

A scalar network analyzer (SNA), which directly drives a millimeter-wave source module to 110 GHz in waveguide, has been used to produce monochromatic, linearly polarized radiation[10]. The waveguides are built such that only the fundamental mode TE_{10} can propagate within the frequency band 75 - 110 GHz. A chopper to modulate the CW signal and a horn antenna to collect radiation on the second waveguide are inserted between the optical elements resulting in the interruption of the transport line as shown in Fig. 3.15, causing the emitted power to be strongly dependent on the frequency as shown in Fig. 3.16.

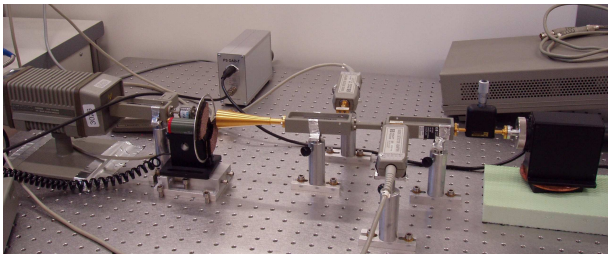

Figure 3.15: Experimental setup for the Golay cell calibration using coupled oscillators.

Figure 3.16 clearly shows the effect of the horn antenna, which behaves as a cavity, on the source power spectrum: the better the alignment of the

[10]Collaboration with the University of Milano-Bicocca, Department of Physics.

optical components the worst the response is, being the oscillations wider. They were attenuated by introducing a misalignment between the horn and the optical axis (blue curve) and measurements were performed with this configuration.

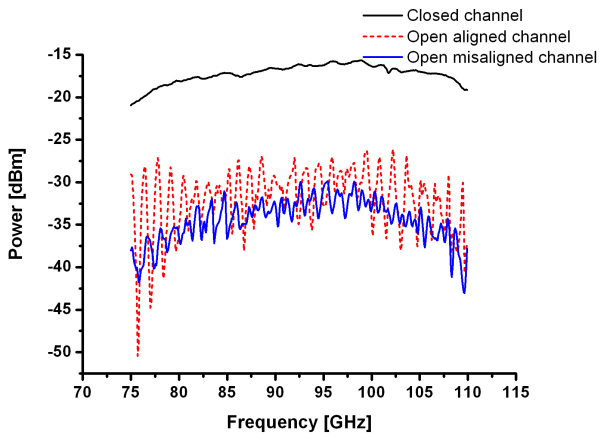

Figure 3.16: Source power spectrum for open (aligned and misaligned) and close channel.

To reduce power losses and to ensure an almost perfect RF contact, thus preventing reflected power and resonance effects, a conical tapered waveguide with aperture 30^o has been studied (HFSS[11] code) and manufactured from an anticorodal[12] rod by electroerosion to have at one end a standard flange with rectangular aperture ($x = 2.54\ mm$; $y = 1.27\ mm$) and a custom circular flange with radius of 3 mm to match the detector window at the other end.

An initial power of 0 dBm has been attenuated and chopped at 10 Hz and fed to a lock-in amplifier to eliminate the background noise. The frequency has been swept over 75 - 110 GHz band in 0.1 GHz steps. The responsivity, defined as the ratio between the measured voltage response and the incident power, is shown in Fig. 3.17.

On average, the responsivity has a reasonable almost flat behaviour. The peak amplitude is strongly dependent on the aperture between the waveguides necessary for chopping and are not a detector characteristic. Finally, the order of magnitude of the measured cell responsivity is in good agreement with the manufacturer specifications.

[11]HFSS is a 3D electromagnetic fields simulation tool.

[12]Aluminum alloy.

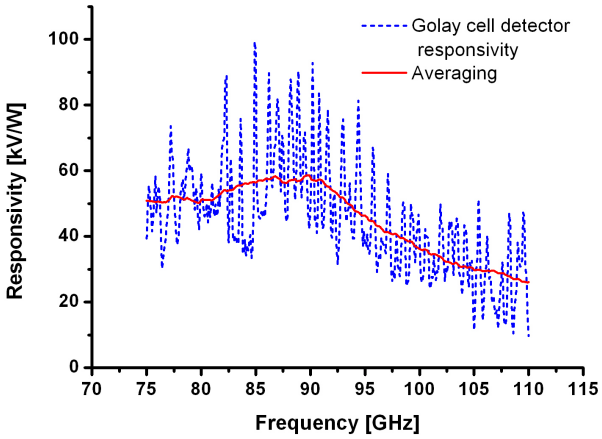

Figure 3.17: Golay cell detector responsivity.

More details on the calibration of tapered waveguides, network analyzer and attenuator can be found in Appendix C.

3.5.2 Hot-Cold Method

In microwave radiometry, calibration is commonly performed comparing liquid nitrogen cooled to room temperature black body-like sources.

The method, called hot-cold, gives a broad band calibration. In order to get a point-to-point calibration band-pass filters have to be inserted to select a specific wavelength. Finally, to reduce the power reaching the detector and to cut visible and near-infrared (NIR) contribution, additional low-pass filters have to be used.

If we assume a blackbody having the physical temperature T, the radiation intensity, $BB(\nu, T)$, can be calculated according to Planck's law, Eq. 3.7:

$$BB(\nu, T) = \frac{2h\nu^3}{c^2} \frac{1}{e^{\frac{h\nu}{kT}} - 1} \tag{3.7}$$

where k is the Boltzmann constant, c the speed of light, ν the radiated frequency, h the Planck's constant.

The power emitted by a blackbody source is given by integrating over the whole frequency spectrum the following expression

$$P(\nu, T)d\nu = A\Omega BB(\nu, T)d\nu = A\Omega \frac{2h\nu^3}{c^2} \frac{1}{e^{\frac{h\nu}{kT}} - 1} d\nu \tag{3.8}$$

By taking into account the solid angle subtended by the detector (Fig. 3.18), which can be estimated from Eq. 3.9

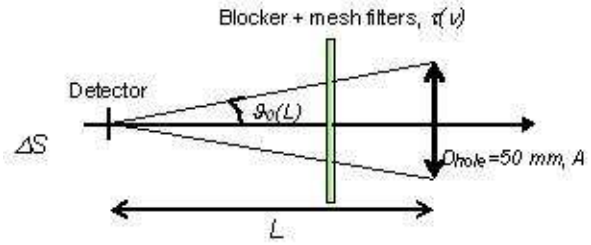

Figure 3.18: Experimental geometry.

$$\Omega(L) = \int_0^{2\pi} \int_0^{\vartheta_0(L)} RA(\vartheta, \phi) \sin\vartheta \cos\vartheta, d\vartheta d\phi \tag{3.9}$$

and the emission spectrum (3.7), the power ΔP on the detector can be calculated by means of Eq. 3.10:

$$\Delta P = A\Omega \int \Delta BB(\Delta T, \nu)\tau(\nu)d\nu \tag{3.10}$$

where $\Delta BB(\Delta T, \nu) = BB(T_{hot}, \nu) - BB(T_{cold}, \nu)$ is the brightness difference between the two sources, A is the effective emitting source area and $A\Omega$ the radiation throughput that is a measure of radiating energy transported by the beam; $\tau(\nu)$ is the transfer function which takes into account blockers, to stop the visible and NIR light, and mesh filters, to select the wavelength of interest. L is the distance between the detector and the source and $RA(\vartheta, \phi)$ the measured detector angular response (Fig. 3.19) which, assuming cylindrical symmetry, depends only on ϑ.

Infrared detectors are usually only sensitive to variations of illumination, therefore a chopping setup is used.

The hot-cold calibration method considered[13] uses two blackbody sources made of ECCOSORB[14], the hot one at room temperature (300 K) directly

[13]Collaboration with the University of Rome "La Sapienza" - Physics Dept.

[14]Sheet of silicon rubber impregnated with iron compounds whose magnetic permeability, μ is close to its dielectric constant ε, so that its impedance tends to $Z = \sqrt{\frac{\mu}{\varepsilon}} = 377\ \Omega$, i.e. the vacuum impedance (Emerson & Cuming Microwave Products - `www.eccosorb.com`)

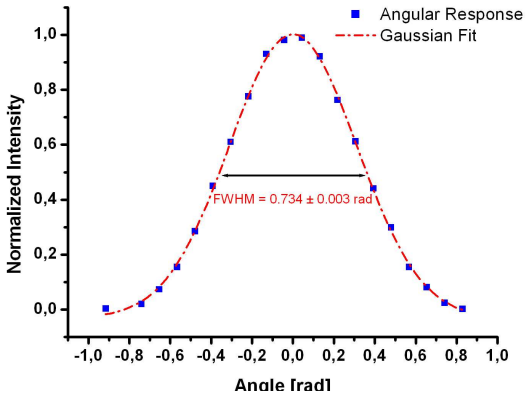

Figure 3.19: Golay cell detector measured angular acceptance.

attached to the chopper wheel, and the cold one floating in liquid Nitrogen at 77 K [36], the difference signal being measured.

Isolating part of the spectrum using proper band-pass filters[15] with center wavelengths of 850 μm, 1.1 mm, 1.4 mm, 2.1 mm (between 10 to 15% of tolerance) allows a responsivity measurement at different wavelengths, but at temperatures for which there is sufficient intensity in the far-infrared range of interest, the spectrum rises steeply towards short wavelengths as $1/\lambda^4$, requiring efficient blocking. Since even a small leakage at NIR and visible wavelengths would dominate any signal measured, low-pass filters, like Yoshinaga[16] ($\hat{\nu}_{cutoff} = 55\ cm^{-1}$) and Fluorogold[17] ($\hat{\nu}_{cutoff} = 30\ cm^{-1}$, 3 mm thick) have been inserted. Theoretical transmission curves for all these filters are shown in Fig. 3.20, their calibration being missing.

The detector is positioned at a distance from the source of 3 cm and the output voltage ΔS recorded (Fig. 3.21) for each wavelength selected by the free-standing mesh filters. With careful consideration of the geometry even an absolute value of the detector responsivity as function of frequency can be calculated from Eq. 3.6.

The large signal at 143 GHz (red dots and green triangles), corresponding to the 2.1 mm mesh filter, is due to the wide mesh of the filter for long wavelengths, resulting in a greater contribution of leaking short wavelengths. With more blockers the leakage is reduced and complete attenuation of the visible light contribution (blue squares) is achieved if a fluorogold filter is also added, resulting in a flat frequency response within the errors.

[15]Free-standing mesh filters manufactured by IKI in Moskow, cf. [37].

[16]It is made from polyethylene sheets loaded with varieties of powdered crystals.

[17]It is a form of glass-filled Teflon.

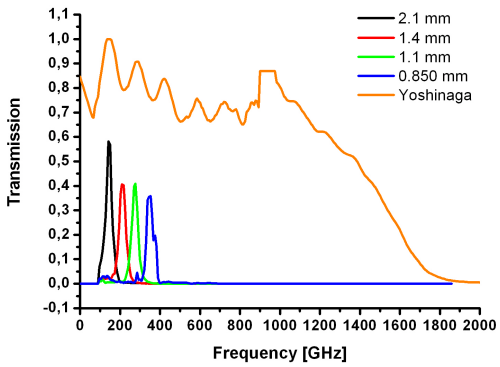

Figure 3.20: Transmission curves of the band-pass and low-pass filters used.

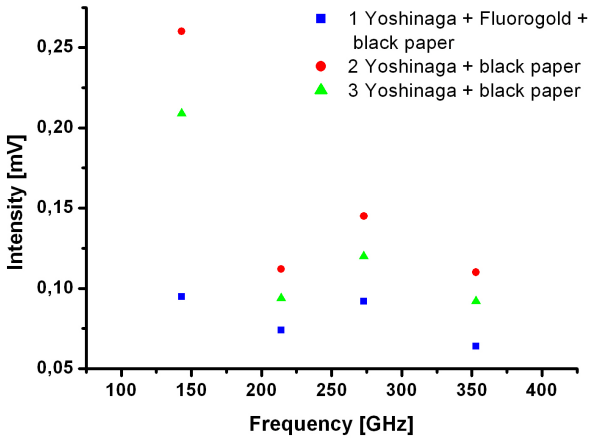

Figure 3.21: Detector output voltage with different blockers.

High-Resolution Diamond Transmission

From literature [45], we know that a non-wedged diamond window of thickness $d = 0.46\ mm$ and refractive index $n = 2.4$ can produce interference fringes with period $\hat{\nu} = \frac{1}{2nd} = 5\ cm^{-1}$, as shown in figure 3.22, and visible in the high-resolution transmission function.

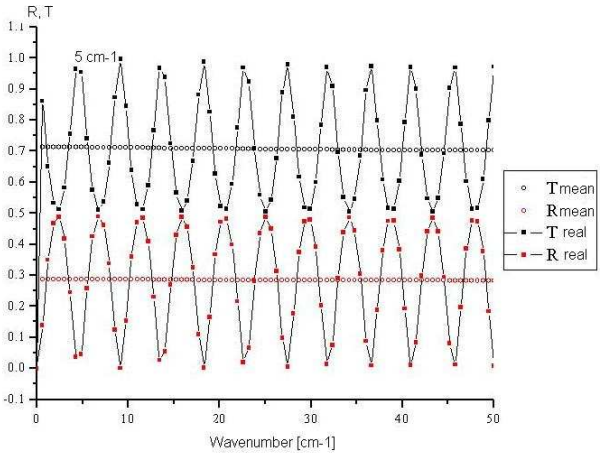

Figure 3.22: Transmittivity and reflectivity for a plane-plane faces diamond window of thickness $d = 0.46\ mm$ and refractive index $n = 2.4$.

To check the presence or not of these structures on the Golay diamond window, a high-resolution measurement has been performed using a Mercury vapor lamp[18] and a lamellar grating interferometer [38], [39], whose efficiency is well-known.

The radiation from vapor lamp, operating at 3 atm, goes through the lamellar grating interferometer. Interference effects occur if the radiation, coming from the source, is reflected by two sets of mirror blades which can be shifted one with respect to the other to vary the distance h, responsible for the path difference in the beam proportional to $2h$. The spacing between

[18] In the visible-UV range it is characterized by an arc emission due to the electric discharge through the Hg vapor, while in the FIR/mm-waves it is similar to a blackbody emission, due to the inner quartz bulb, at a temperature between 3000 K and 3500 K. The total spectrum is then given by the overlap of both types of emission and for this reason it is not well-known.

the inner and outer face can be varied by means of a stepper motor; the step width between both faces and the acquisition time can be fixed in advance. The radiation, modulated by a chopper at a frequency of 12.5 Hz locked to a lock-in amplifier, is then directed to the detector window. The output signal is then acquired with a LabView program and analyzed by means of Fourier spectroscopy by extracting the transmission spectrum of the detector window from the interferograms.

Figure 3.23 shows a scheme of the lamellar grating interferometer and its optical configuration.

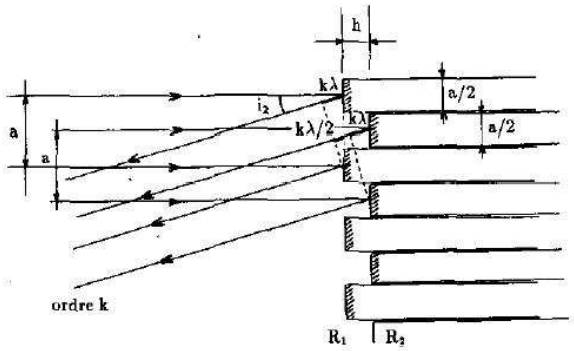

Figure 3.23: Sketch of a lamellar grating interferometer.

The scanned frequency range is $0 - 31\ cm^{-1}$, which is equivalent to the wavelength range from infinite up to 300 μm; the spectral resolution is $\Delta\hat{\nu} = \frac{1}{d_{max}} = 0.5\ cm^{-1}$, d_{max} being the maximum travel of the moving blade. The mechanic interferometer step is 80 μm over 20.48 mm total length. The zero-path-difference (ZPD), corresponding to the position where mirrors are coplanar and resulting in a maximum signal, has been calibrated to be roughly at the position of half the total number of steps. This measurement does not provide an absolute calibration, at this purpose two spectra are needed, indeed: one spectrum recorded with the filter, the second one without any filter. However, in the present case, the filter is given by the Golay cell detector window, thus only a relative calibration can be obtained. Again blocking filters are necessary to cut the non-negligible UV and visible contribution coming from the arc emission of the Mercury vapor lamp; at this purpose, a Yoshinaga blocker has been used. Since the signal is extremely weak a second filter, a hot-pressed polyethylene (PE) filter with 15 cm^{-1} cut-off, was necessary to decrease the frequency band and increase the signal-to-noise ratio.

Ten interferograms have been acquired and fast Fourier transformed by

means of an IDL 5.4 program to determine the high-resolution transmittance for the Golay cell diamond window. In figure 3.24 the average spectrum is shown as function of the wavenumber. The low-frequency cut-off depends on the lamellar grating interferometer geometry, while the high-frequency cut-off is given by the PE filter.

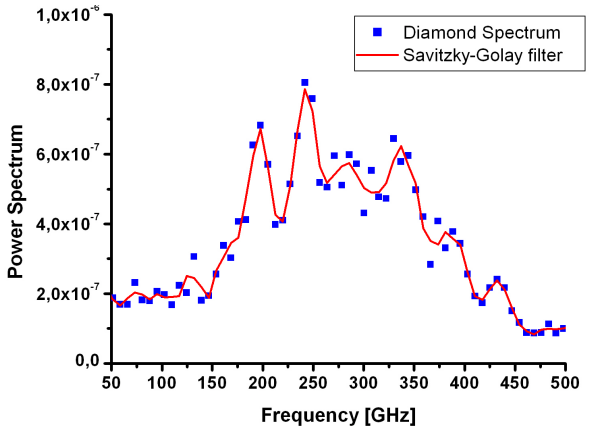

Figure 3.24: High-resolution diamond spectrum.

No interference fringes with the expected period of roughly 150 GHz are evident in the high-resolution spectrum. Thus, the diamond window does not give rise to interference effects due to the parallel flat surfaces. However, the diamond spectrum presents some structures with sharp peaks at 196 GHz, 241 GHz, 286 GHz and 336 GHz, with 45 GHz spacing, except for the last one spaced of 50 GHz. These structures are not due to the Yoshinaga filter used since the characteristic ringing in the low-frequency region of the transmission function (Fig. 3.20) does not show the same spacing, but they might be due to the polyethylene hot-pressed filter whose transmission function is unknown.

The fact that the spectral resolution of the Martin-Puplett interferometer, used in the bunch length measurement, is greater than the spacing between the peaks in the diamond spectrum allows to disregard these structures by fitting the curve with a flat function in the range $200 - 350$ GHz.

3.5.3 FEL Radiation Source

A quasi-monochromatic radiation source with known intensity, provided by the far-infrared free-electron laser FELIX[19], has been used to look at the Golay cell detector response in the range 100 160 μm.

The FEL intensity was monitored with a reference joulemeter, whose calibration constant, 573 V/J, is assumed to be valid over the full measurement, and regulated to a suitable value by means of attenuators between 0 and 38 dB. Frequency dependencies of both attenuators and reference detector cannot be separated in the results.

The setup is shown in Fig. 3.25.

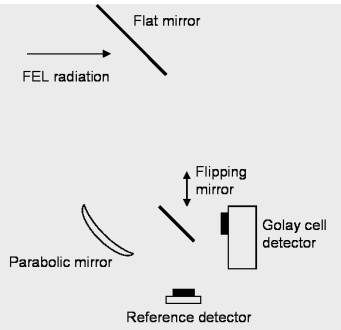

Figure 3.25: FELIX experimental setup.

At 135 μm and with 3 dB attenuation a pulse energy of about 9 μJ can be estimated from the joulemeter measurement. With 30 dB attenuation, the energy measured with the joulemeter was roughly 18 nJ and the detector signal amplitude on the oscilloscope 30 mV. A sensitivity of 1.7 MV/J then follows.

The signal was observed on the oscilloscope. Scans over the wavelengths were made via a LabView program and GPIB readout of the scope. Fig. 3.26 shows two scans made under normal pressure in air. The Golay cell detector sensitivity shows a flat behavior over almost the entire range except for a sharp peak at 101 μm in the measurement labelled with number 2, which might be due to instability of the machine, a second measurement, labelled with number 1, performed immediately after this one does not show indeed any particular structure.

[19]FOM Rijnhuizen Institute, Netherlands

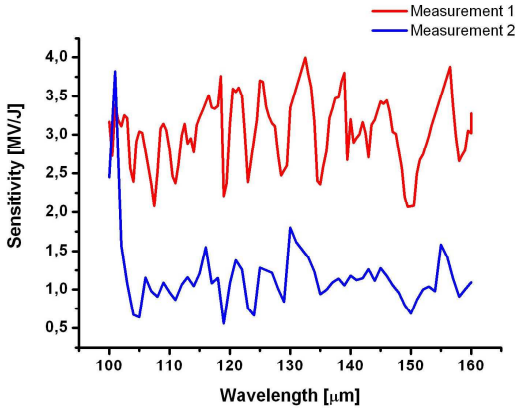

Figure 3.26: Two measurements of the Golay cell detector sensitivity repeated under the same machine conditions.

3.6 Calibration Results

The detector characterization, performed in the three different regions of the spectrum, from 100 μm to 4 mm, do not show any significant structures in the detector response as expected from the Golay cell specifications which though are given up to 1 mm and based on the low-resolution (intereference free) diamond transmission curve.

In all the measurements, the experimental geometry and the optics used to reduce intensity, block high-frequencies and collect radiation contribute to the detector response more than the detector itself, resulting in a responsivity curve which is not flat in frequency, the frequency dependence being determined by the experimental setup. In most cases, for example in the calibration described in section 3.5.1, it is not possible to correct for this contribution since the effect caused by the aperture in the waveguides section on the power distribution can be neither estimated nor removed. However since the described frequency-dependent behavior comes from the experimental setup, it is acceptable to fit the results with a flat, with respect to the frequency, function. The total Golay cell detector transfer function, shown in Fig. 3.27, has therefore been obtained by interpolating the transfer function coming from each calibration method, the most confident ones being those using hot-cold and FEL radiation due to the much easier experimental geometry.

The high-pass filter behavior is shown, the intermediate region (0.5 - 2 THz) being however not covered by any calibration method. This first-

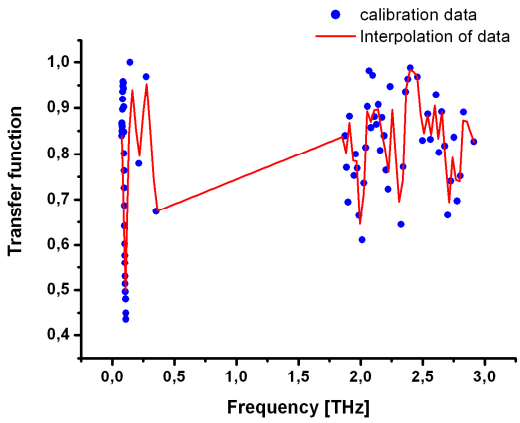

Figure 3.27: Golay cell transfer function in the range 100 μm - 4 mm.

time Golay cell characterization extends however to the long wavelength region of the spectrum, providing a good understanding of how it works and giving a sufficient response for what concerns the bunch length measurement correction.

Chapter 4

The Bunch Length Characterization

As already stressed in chapter 2, a measurement of the coherent diffraction radiation pulse length is also a measurement of the longitudinal size σ_b of the electron bunch if, in case of off-axis observation, the transverse beam size ρ and the observation angle θ satisfy condition 4.1

$$\frac{2\pi\rho\tan\theta}{3.83} \ll \sigma_b \tag{4.1}$$

a correction being needed otherwise. We assume the condition always valid.

Since picosecond electron bunches radiate more coherent millimeter and sub-millimeter radiation than longer bunches, the relative electron bunch length can be minimized by simply adjusting the beam injection parameters while monitoring the intensity of the coherent diffraction radiation detected, used as fast monitor to check if the compression has taken place. The analysis of the coherent diffraction radiation spectrum, based on Fourier transform spectroscopy, will give an accurate, except for a phase factor, characterization of the pulse shape. The Kramers-Kronig relations will be therefore needed to cancel the ambiguity of retrieving the bunch profile from the measured CDR spectrum.

Spectral techniques avoid the synchronization difficulty typical of time domain methods, but they suffer similar losses of low-frequency components, due to diffraction, finite size of the radiator and reduced acceptance and sensitivity of detectors at long wavelengths. Furthermore, only certain classes

of bunch shapes can be accurately reconstructed from their power spectra.

Measurements have been performed at the TTF VUV-FEL linac downstream from the second bunch compressor (BC3) varying the electron energy and energy spread in the compressors by changing the accelerating sections RF phase. Both bunch compressors (BC2 and BC3) have been used in on-crest and off-crest operation. A few measurements have been done during SASE FEL operation (see section 4.2.4) to demonstrate the effective non-destructive nature of diffraction radiation with different slit apertures.

The CDR signal detected by the Golay cell detectors is read out by an analog-digital converter (ADC), triggered by the VUV-FEL macropulse trigger with a frequency of typically $2-5\ Hz$. Interferograms have been acquired by means of a MatLab scan tool named MIST[1], which allows also the accurate evaluation of the autocorrelation spectrum by fast Fourier transforming (FFT) the normalized (to the total intensity) difference interferogram and the reconstruction of the bunch profile, corrected by quartz window, interferometer and detector transfer functions.

4.1 Interferogram Acquisition

The interferogram is obtained by recording a certain number, depending on the beam stability, of signal amplitudes from both Golay cells detecting the horizontal, $V_h(x)$, and vertical, $V_v(x)$, polarization as a function of the path difference, x, in the two arms. The single data point of the raw interferogram (Fig. 4.1) is given by the mean value of these measurements, its statistical error is the standard deviation.

Figure 4.1, showing the raw interferogram from both the horizontal and vertical polarization detectors, allows a first adjustment of the interferometer misalignment, denounced by a non-symmetric interferogram, and of the response of the detectors, whose sensitivities are slightly different due to a different readout electronics (built-in pre-amplifier and impedance adaptor circuits). Non-symmetric interferograms could also occur because of an improper beam optics, resulting in the beam to be intercepted by the diffraction radiation target, as Fig. 4.3 shows.

This effect largely affects the spectra, resulting in a double peak for the curves at $+3\ deg$ and $+6\ deg$ as shown in Fig. 4.2.

The measured voltage is therefore corrected to allow the normalization to the total intensity.

[1] **M**artin-Puplett **I**nterferometer **S**can **T**ool written by Lars Fröhlich - DESY.

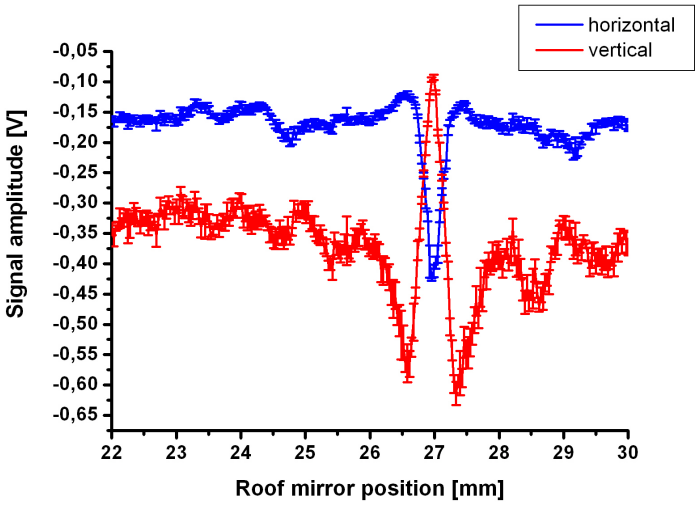

Figure 4.1: Raw interferogram from horizontal and vertical polarization detector.

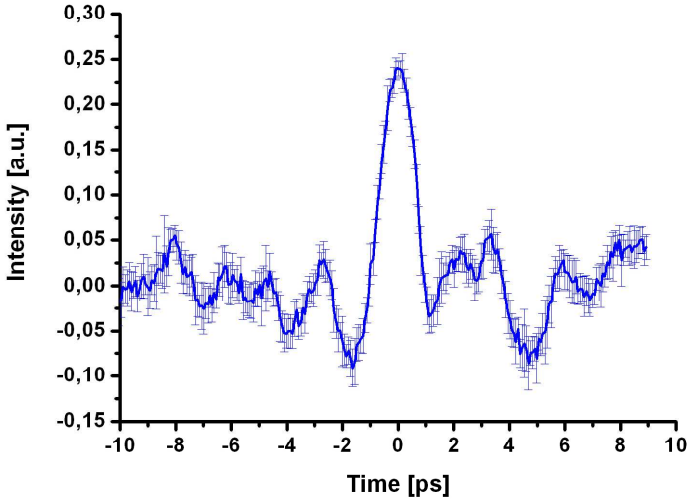

Figure 4.2: Normalized difference interferogram in case the beam is intercepted by the target.

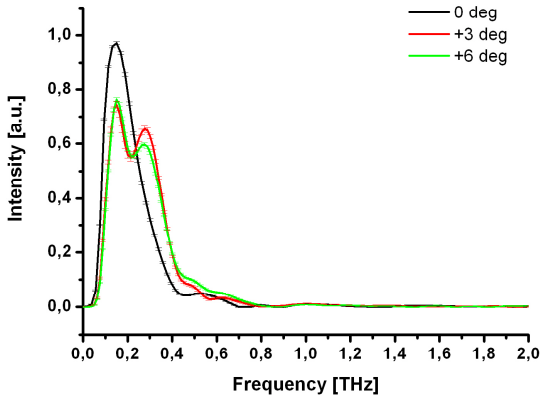

Figure 4.3: Coherent diffraction radiation spectra measured for different accelerating phases. The curve labelled as +3 *deg* is obtained by Fourier transforming the interferogram of Fig. 4.2.

Before starting each set of measurements, the signal from the toroids (Fig. 4.4) is used to ensure that transport of the beam through the linac is optimized and that the beam is not intercepted by our target.

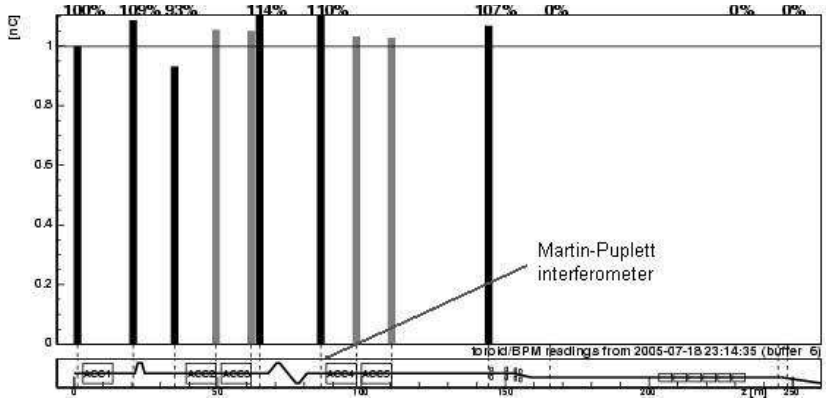

Figure 4.4: Toroids reading.

After that, a phase scan of the accelerating module of interest for the measurement is made recording the signal of both bunch compression monitors, one placed downstream from BC2 and the other downstream from BC3, and the Golay cell detector mounted on the interferometer at BC3 in order

to check the RF phase value for which the compression is maximum (Fig. 4.5).

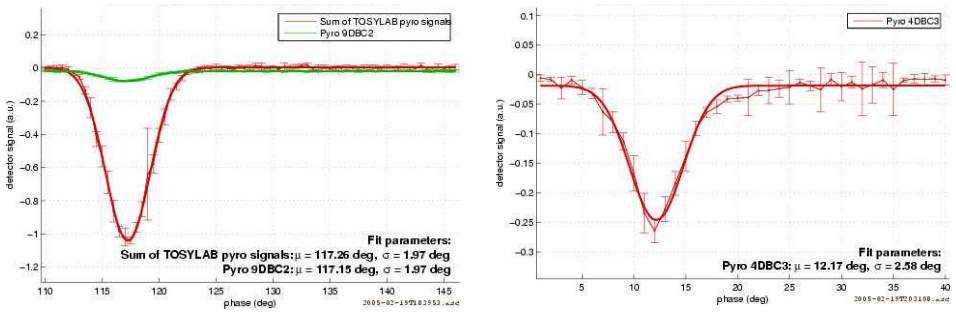

(a) BC2 (b) BC3

Figure 4.5: Accelerating module phase scan.

Several tests have been performed to optimize the detector response with different sets of beam parameters.

In the measurements discussed in the following section, 0.3 nC and 1 bunch have been used because of the peculiar Golay cell response. Either for high charge or high peak current beam, indeed, the characteristic Golay cell damping oscillations (of the order of μs), already discussed in chapter 3, saturate giving rise to a triangular shape signal as shown in figure 4.6, where the maximum signal amplitude is not well distinguished anymore. As a consequence, due to the slow temporal response of the Golay cell detector, the time interval scale of the fast ADC used is comparable with the period of the detector damping oscillations, resulting in a wrong sampling of the ADC.

To operate either at higher current or higher charge, the ADC has to be changed and its temporal interval scale set to match with the Golay time response scale.

4.1.1 Interferogram Fitting Function

Since the full width at half maximum (FWHM) of the autocorrelation function is directly proportional to the FWHM of the pulse[2], a rough analysis can

[2]For a Gaussian shape beam the FWHM is $1/\sqrt{2\pi}$ times the FWHM of its autocorrelation and for a rectangular pulse is exactly the FWHM of its autocorrelation.

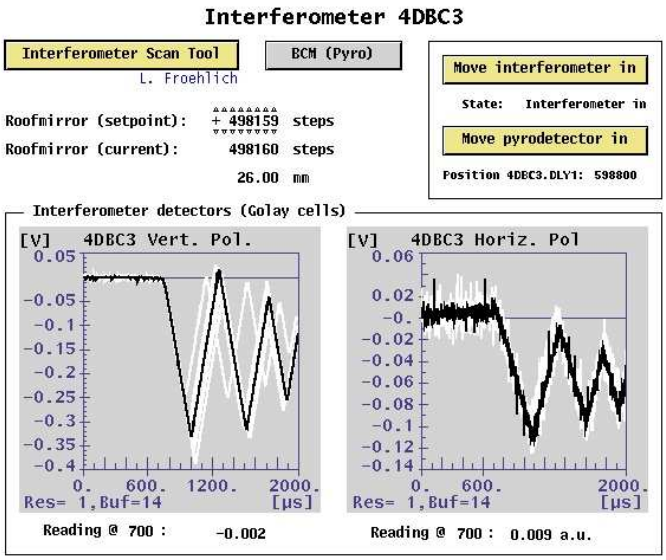

Figure 4.6: Saturation of the characteristic Golay cell detector ringing around the maximum signal. 6 bunches, 1 nC per bunch.

be done by assuming the pulse shape is known. Fitting the normalized difference interferogram, it is possible to find the rms beam pulse length and the cut-off frequency of the interferometer [41]. Before proceeding in the research of the best interferogram fitting function for both Gaussian and real TTF bunch profile, it is worthwhile to note the high-pass filter behavior of the interferometer due to diffractive losses and physical apertures in the detecting system: an analytical filter function, which well describes the interferometer effect on the spectrum, is of the form

$$g(\omega) = 1 - exp(-\xi^2\omega^2) \tag{4.2}$$

where ξ is the intereferometer cut-off parameter. The high-pass filter behavior is justified also by the simulation shown in chapter 3.

In the following subsections, we will derive the interferogram fitting function first assuming a Gaussian electron beam profile, then considering the true TTF beam pulse whose shape has a sharp asymmetric peak with a long tail.

Gaussian Bunch Shape

The easiest to treat and most widely used assumption made to approximate the true bunch shape is that it is a Gaussian with a charge density distribution given by

$$\rho(t) = \frac{1}{\sqrt{2\pi}\sigma_t} \exp\left(\frac{-t^2}{2\sigma_t^2}\right) \tag{4.3}$$

In the frequency domain, calling $g(\omega)$ the high-pass filter function of the interferometer, the autocorrelation of the signal is given by the product of the spectral beam density, $\rho(\omega)$ and $g(\omega)$ as

$$\rho_f(\omega) = \rho(\omega)g(\omega) \tag{4.4}$$

and the spectrum of the signal is

$$I_{fit}(\omega) \propto |\rho_f(\omega)|^2 = |\rho(\omega)|^2(1 - 2e^{-\xi^2\omega^2} + e^{-2\xi^2\omega^2}) \tag{4.5}$$

The signal in the time domain is therefore obtained by inverse Fourier transforming Eq. 4.5

$$\delta(\tau) \propto \left[e^{-\frac{(\tau-\tau_0)^2}{4\sigma^2}} - \frac{2\sigma}{\sqrt{\sigma^2+\xi^2}} e^{-\frac{(\tau-\tau_0)^2}{4(\sigma^2+\xi^2)}} + \frac{\sigma}{\sqrt{\sigma^2+2\xi^2}} e^{-\frac{(\tau-\tau_0)^2}{4(\sigma^2+2\xi^2)}}\right] \tag{4.6}$$

For a Gaussian beam the rms beam pulse length, σ, and the cut-off frequency of the interferometer, ξ^{-1}, are found simply fitting Eq. 4.6, called from now on "3-Gaussian" function, to the time domain interferogram.

Results of this "3-Gaussian" fit are compared in section 4.2.1 to those of a standard Gaussian fit. The interferometer frequency cut-off, $\xi^{-1} \simeq 150\ GHz$, obtained by the "3-Gaussian" fit is confirmed by both experimental results and simulations as shown in the measurements section and in chapter 3, respectively.

True TTF Bunch Shape

From simulations, supported by time domain bunch length measurements [42], the TTF VUV-FEL compressed bunch profile is predicted to have a very sharp, asymmetric peak and a long tail as shown in Fig. 4.7, due to the non-linear energy-phase correlation introduced by the off-crest acceleration during bunch compression, as already discussed in chapter 3.

Both the high and low frequency cut off, introduced by the frequency domain technique using DR diagnostics, result in a more complicate reconstruction of the bunch profile.

The high frequency cut off, produced by the slit aperture and the z-cut quartz window transmission, could in principle affect pulses such the true TTF ones, because the peak, which highly contributes to the FEL lasing, contains much larger high frequency components than low frequencies. However, frequency domain techniques introduce a more severe suppression of low frequencies which correspond to slow variations and are related to the tail. The loss of information on the tail does not affect the FEL generation.

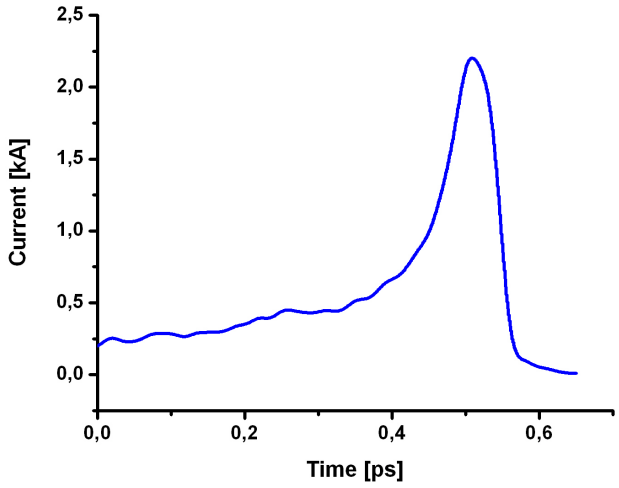

Figure 4.7: Expected TTF bunch profile.

The function which best fits the true pulse is

$$\rho(t) = \rho_0 + A\Big[1 - \exp\Big(-\frac{t-t_0}{q_1}\Big)\Big]^p \exp\Big(-\frac{t-t_0}{q_2}\Big) \tag{4.7}$$

with t_0 such that $t_1 = t_0 + q_1[\ln(pq_2 + q_1) - \ln(q_1)]$; s_0, A, t_0, q_1, q_2, p being the fitting free parameters.

The fitting curve for the interferograms, assuming a pulse whose shape is shown in Fig. 4.7, is then found by Fourier transforming equation 4.7,

$$\tilde{\rho}(\omega) = \int_{-\infty}^{\infty} \rho(t) \exp(-i\omega t) dt, \tag{4.8}$$

convoluted with the high-pass filter function of Eq. 4.2. The resulting power spectrum is then given by

$$I_{fit}(\omega) = \tilde{\rho}(\omega)^* \tilde{\rho}(\omega) |1 - \exp(-\xi^2\omega^2)|^2 \tag{4.9}$$

The interferogram fitting function, shown in Fig. 4.8, is then given by Fourier anti-transforming equation 4.9

$$\delta(\tau) = \int_{-\infty}^{\infty} I_{fit}(\omega) \exp(i\omega\tau) d\omega \tag{4.10}$$

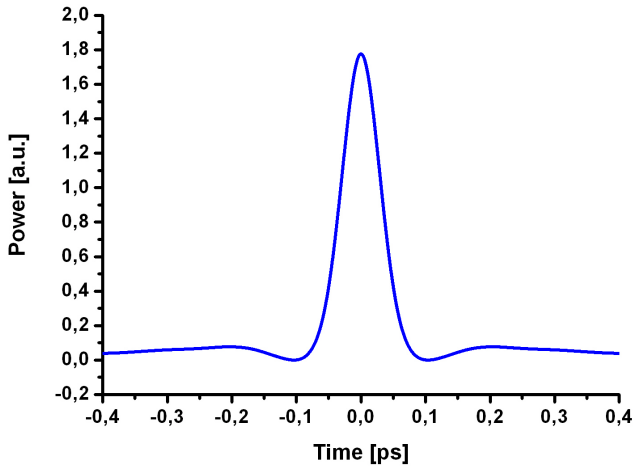

Figure 4.8: Interferogram fitting function for the true pulse shape.

4.2 Bunch Length Measurements

Several measurements have been performed under different machine conditions.

In this section we want to show the bunch profile dependence on both accelerating modules phase. For this purpose several scans have been done varying ACC2-3 phase around the maximum compression value, while ACC1 is tuned on crest.

The spectra have been corrected by the Golay cell detector transfer function, obtained from calibration, the z-cut quartz window and the interferometer transfer functions, obtained from the simulation with the THz Transport code as described in chapter 3.

The final bunch profile has been determined by first evaluating the measured CDR power spectrum by Fourier transforming the autocorrelation function as described in the previous section. The power spectrum from a bunch

of N electrons, defined in chapter 2, allows to derive the bunch form factor once the single-particle power spectrum is known. Finally, the bunch profile is determined by anti-transforming the form factor and applying the Kramers-Kronig method to retrieve the proper phase factor as described in chapter 2.

4.2.1 Bunch Length Dependence on the $ACC2-3$ Phase

Four interferograms have been taken by keeping fixed the $ACC1$ accelerating phase at the on-crest value (128.61 deg) and varying the $ACC2-3$ phase around the maximum compression value found with the pyro-detector phase scan at 12 deg. The energy measured at the exit of the third accelerating module is 380 MeV. One bunch with 0.3 nC per bunch has been used.

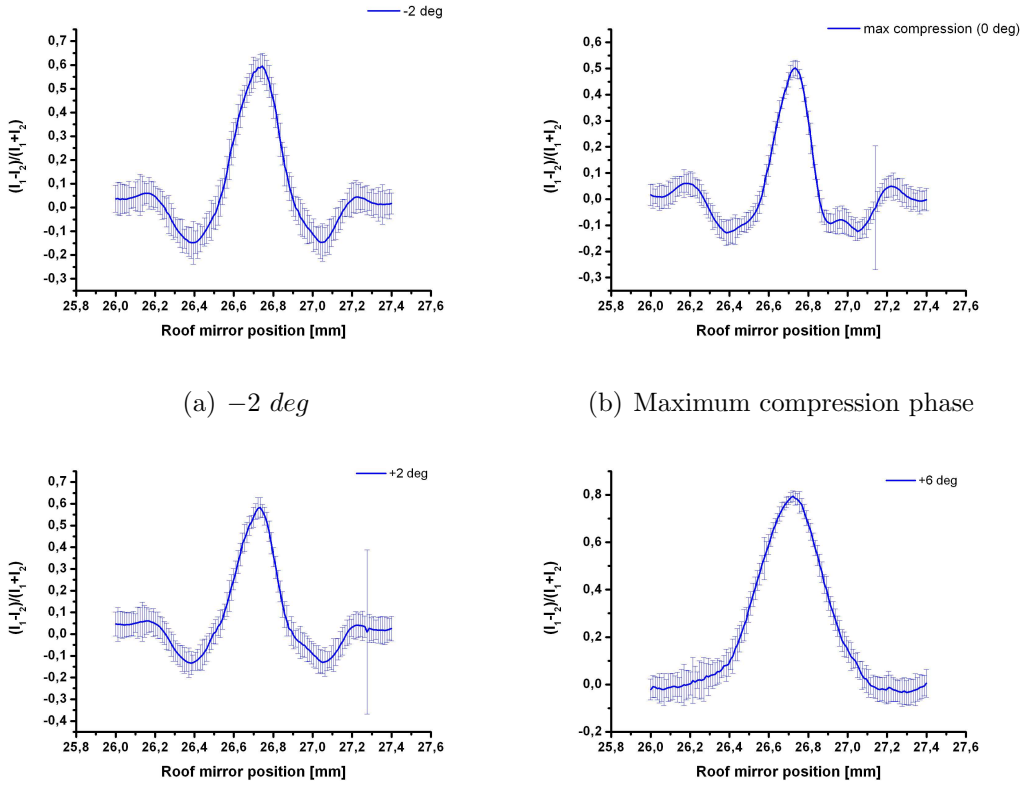

(a) -2 deg

(b) Maximum compression phase

(c) $+2$ deg

(d) $+6$ deg

Figure 4.9: Interferograms for different $ACC2-3$ accelerating module phases.

The normalized difference interferogram is plotted in figure 4.9 as a function of the path difference for four values of the $ACC2-3$ accelerating module phase. For convenience, the phase corresponding to the maximum compression is arbitrarily set at 0 deg.

Figure 4.9 shows the typical interferogram with the center burst at the zero path difference where all wavelengths are in phase. The difference between the baseline and the depth of the side minima, visible in the plots a), b) and c) of Fig. 4.9, is strictly dependent on the steepness of the electron beam profile, whose slope is steeper the shorter the bunch. The longer the bunch the profile gets smoother and closer to a Gaussian distribution, resulting in the merging of the side minima with the baseline as shown in the plot d). Fig. 4.10 shows the comparison between the four interferograms.

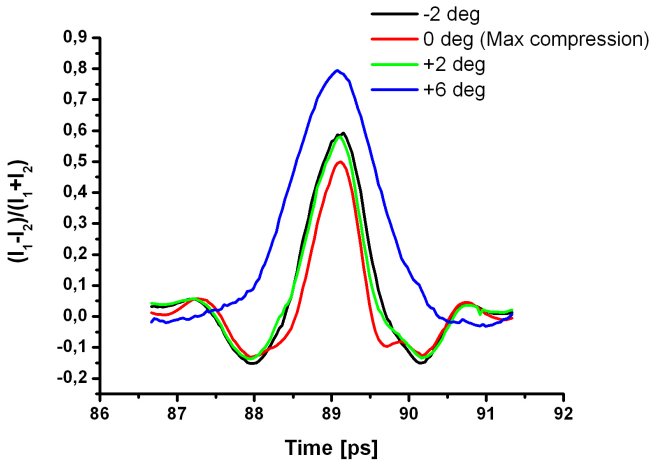

Figure 4.10: Comparison between interferograms with different accelerating phases.

Plotting the bunch length (FWHM) as a function of the accelerating phase (Fig. 4.11a), the curve behavior is in very good agreement with the results obtained from the phase scan curve (Fig. 4.11b).

The black and red curve in figure 4.11 correspond to a first approximation bunch length measurement, determined by fitting the interferograms with a Gaussian and the "3-Gaussian" function introduced in the previous section. The agreement between the curves is within 15%. Corrections due to the detector transfer functions are not taken into account in this first analysis, since it was performed directly on the normalized difference interferogram.

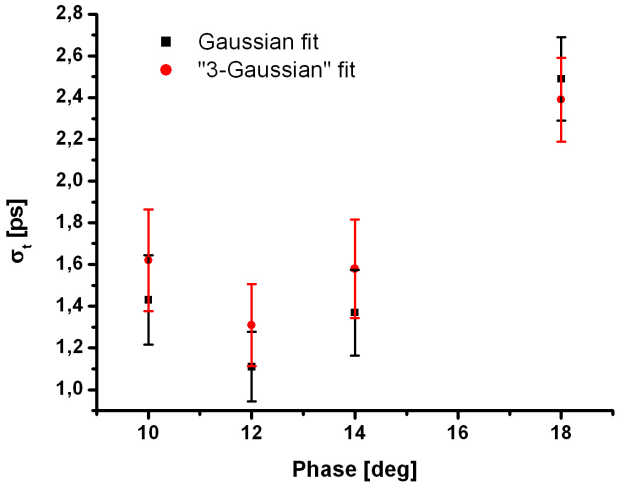

(a) Fit results

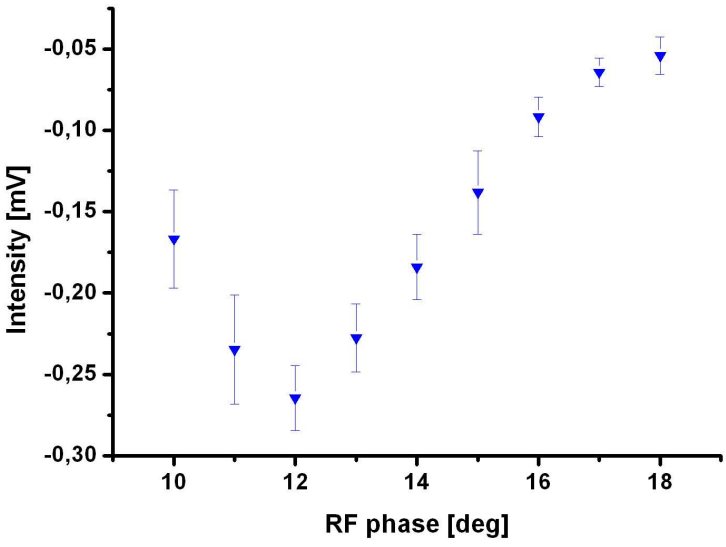

(b) Pyro-scan at BC3

Figure 4.11: Comparison between the bunch length (black and red points in plot (a)) and the phase scan curve (blue triangles in the plot (b)). The bunch length follows very well the phase scan, the maximum registered intensity corresponding to the shortest bunch length.

In what follows corrections due to the Golay cell detector transfer function, the z-cut quartz window transmission and the interferometer acceptance are taken into account and the measured spectra corrected by the total transfer function shown in Fig. 4.12. The resulting bunch length (FWHM) for different accelerating phase is plotted in Fig. 4.16: blues squares refer to the correction given by the quartz window transmission function, red circles to both quartz transmission and interferometer acceptance and green triangles to the transfer function of the whole apparatus including the Golay cell detector response.

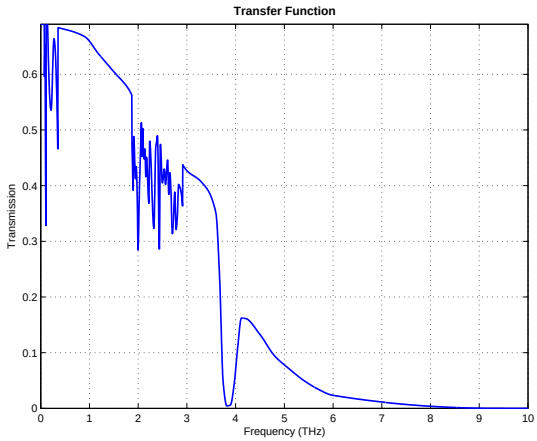

Figure 4.12: Total transfer function taking into account the Golay cell detector response and the z-cut quartz window transmission.

Both the measured spectrum and the form factor show clearly the falling slope is steeper, the longer the bunch, because of the smaller high frequency content. Furthermore, it is evident that the low frequency part of the spectra is strongly suppressed by the detector and the interferometer.

Bunch profiles show a steeply rising slope and a long tail. It is evident that far from compression (blue curve) the profile is wider and more symmetric and both the falling and the rising slopes less steep. At symmetric phases ($-2\ deg$ and $+2\ deg$), the profiles do not appear significantly different because we are close to the minimum where the curve can be very well approximated with a parabola. However, the phase of maximum compression is not a symmetric point for the accelerating field, thus farther from the minimum, the symmetry is broken and also symmetric values of the phase are expected to give different compressions as it is evident from the different slopes in the RF phase scan.

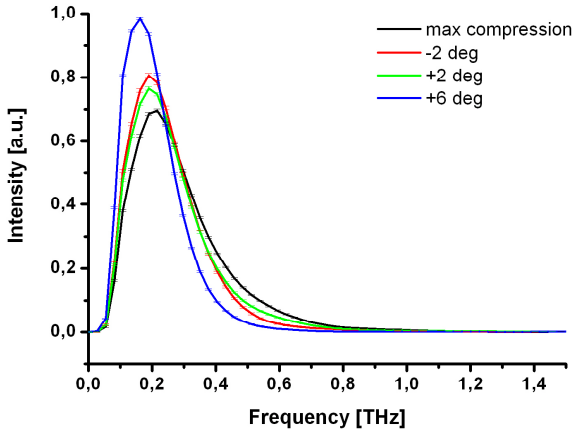

Figure 4.13: CDR measured spectra for different values of ACC2-3 RF phase.

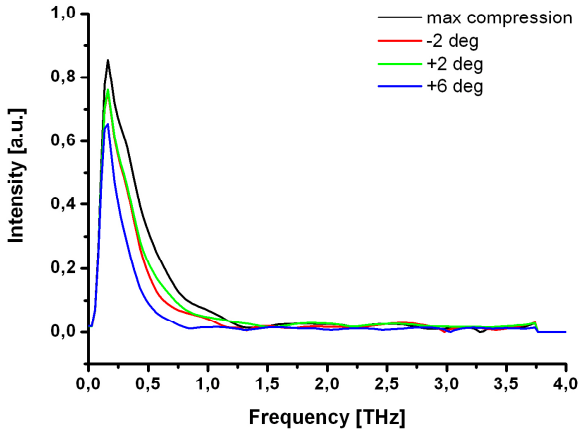

Figure 4.14: Bunch form factor for different values of ACC2-3 RF phase.

An rms bunch length of 0.8 ps is found at the maximum compression phase.

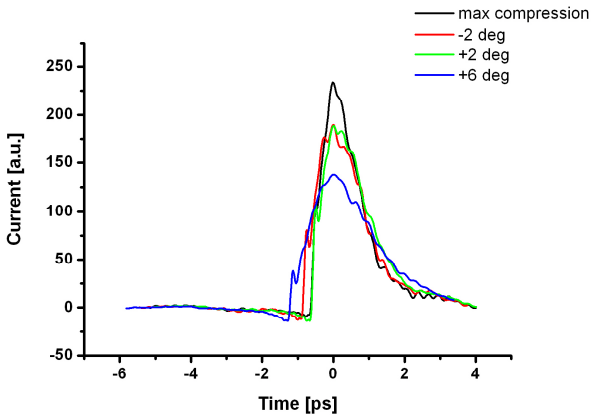

Figure 4.15: Bunch profile for different values of ACC2-3 RF phase.

The width of the shortest peak, obtained by fitting the profile with the function introduced in section 4.1.1, is 1.2 ± 0.1 ps (Fig. 4.17).

Theoretical Evaluation of the Bunch Length

Different particles within the bunch will experience different acceleration depending on the phase of the electric fields they experience as already discussed in chapter 3.1.

Assuming normal longitudinally distributed particles in the beam, the bunch energy spread and the longitudinal emittance can be written in terms of the initial bunch length as

$$\begin{aligned} \sigma_\delta &= \sqrt{\sigma_{\delta_0} + \alpha^2 \sigma_{z,in}^2 + \frac{1}{2}\beta^2 \sigma_{z,in}^4} \\ \varepsilon_z &= \sigma_{z,in}\sqrt{\sigma_{\delta_0} + \frac{1}{2}\beta^2 \sigma_{z,in}^4} \end{aligned} \tag{4.11}$$

with $\sigma_{z,in}$ the initial pulse length, α and β the first and second order energy-length correlation, respectively, defined by

$$\begin{aligned} \alpha &= -\frac{2\pi E_{cav} \sin\phi}{E_0 \lambda_{RF}} \\ \beta &= -\frac{4\pi^2 E_{cav} \cos\phi}{E_0 \lambda_{RF}^2} \end{aligned} \tag{4.12}$$

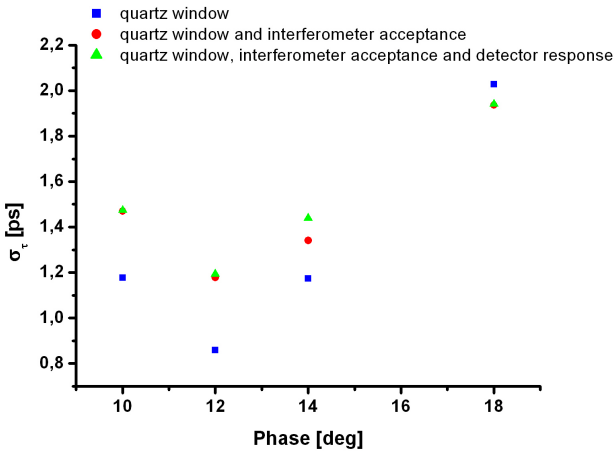

Figure 4.16: Measured bunch lengths (FWHM) for different value of the RF phase. Different curves refer to successive corrections due to the experimental apparatus.

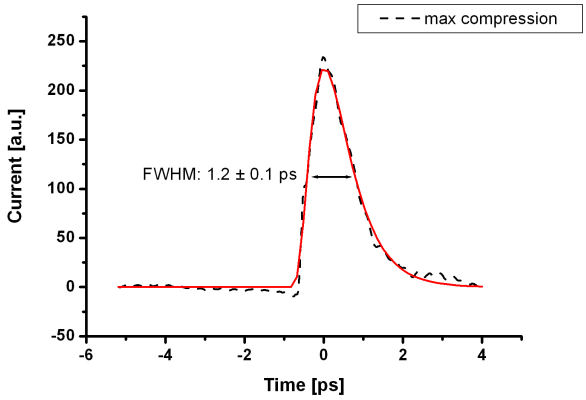

Figure 4.17: The bunch profile corresponding to the shortest bunch is fitted with the function introduced in section 4.1.1.

Assuming a negligible uncorrelated energy spread, the minimum bunch length achievable is given by

$$\sigma_{z,min} = \frac{\sigma_{z,in}^2}{\sqrt{\sigma_{z,in}^2 + \frac{\lambda_{RF}^2}{2\pi^2}\tan^2(\phi)}} \tag{4.13}$$

Knowing that the phase corresponding to the maximum compression is 20 *deg* off crest and $\sigma_{z,in} = 2.2\ mm$, the expected minimum rms bunch length is 0.85 *ps*. Although the calculation does not take into account the uncorrelated energy spread from the injector, the result is in good agreement with the measurement and this should provide us some rough estimates of what to expect.

4.2.2 Estimate of Errors

In the ideal case of no low and high frequency suppression, the CDR spectrum is directly proportional to the bunch form factor from which the longitudinal bunch profile is inferred by means of Fourier analysis. However, the measured spectrum is always affected by the low and high frequency suppression mostly due to the interferometer acceptance. In practice, part of the spectrum, which is assumed to be unperturbed, is selected and the bunch length recovered assuming a known bunch shape. This procedure introduces though a systematic error due to the fact that the portion of the spectrum considered may still be perturbed or that the frequency content is not sufficient to reconstruct the longitudinal bunch profile.

The uncertainty on the bunch length measurement can therefore be evaluated as sum of two contributions: statistic and systematic,

$$\Delta\sigma_z^{tot} = \Delta\sigma_z^{statistics} + \Delta\sigma_z^{systematic} \tag{4.14}$$

the former depending on the beam fluctuations coming from the laser instability (within $\pm 1\ ps$) and on the RF phase stability, the latter being given by the experimental apparatus which introduces a filter whose frequency cut-off makes the reconstruction procedure not precise.

A fluctuation of the laser pulse length of $\pm 1\ ps$ and an instability of the RF phase of 0.01 *deg* may produce an error on the evaluation of the bunch length of 30% as can be inferred by propagating the initial error. However, by averaging on a sufficient number of measurements, the statistical error is significantly minimized.

The systematic error can be partially corrected by calibrating the entire apparatus. This is what we have done at least for the detector whose calibration curve is shown in the previous chapter. As regards the interferometer

acceptance and the quartz window transmission, the total transfer function has been simulated with the THz Transport code, showing a high-pass filter behavior with a cut-off frequency of 150 GHz in good agreement with what found by fitting the interferogram with the "3-Gaussian" function and analyzing the CDR spectra.

The measured bunch length corrected by the total apparatus transfer function shows a very good agreement, within 10%, with the analysis performed on the rough interferograms.

4.2.3 Bunch Length and SASE Signal

Several interferometer scans were performed when the beam was set up to provide FEL laser radiation close to saturation, in order to demonstrate the non-intercepting and non-invasive nature of CDR diagnostics. Fig. 4.18a) shows the history of the FEL intensity generating radiation at 30 nm for both the average and peak photon energy over a long time interval, while Fig. 4.18b) shows the average and peak energy history for each bunch.

The FEL process would be sensitive to any beam perturbation that can derive from wakefields generated on the DR screen by the very high beam current. However during the bunch length measurement no significant disturbance on the FEL radiation has been detected, confirming the effective non-perturbing nature of the technique.

The electron beam energy is 360 MeV, 8 bunches, 1 nC per bunch, are transported. ACC1 and ACC2-3 phase are set at the nominal values to get SASE.

The measured spectra show a noisy behavior due to the fact that the detector signal was noise-dominated.

Substructures, in agreement with what found in [43], are visible in the longitudinal beam profile shown in Fig. 4.20.

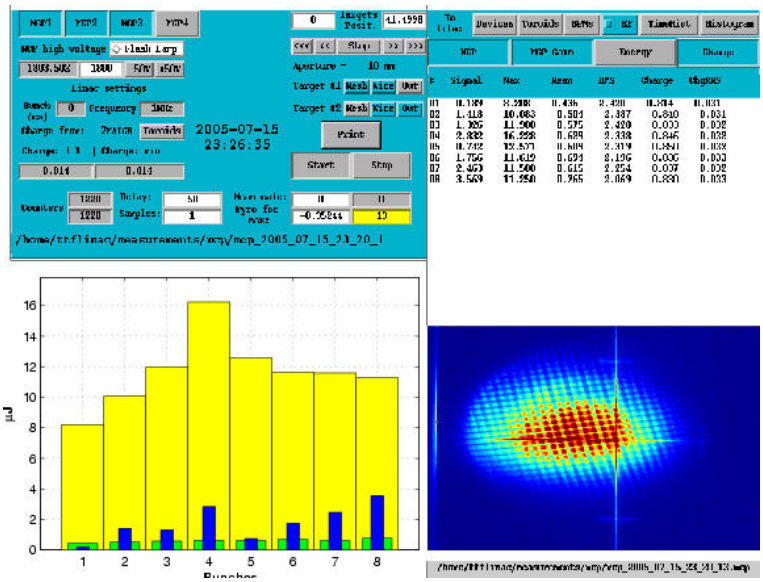

Figure 4.18: Energy history of the SASE operation and snapshot of the radiation spot.

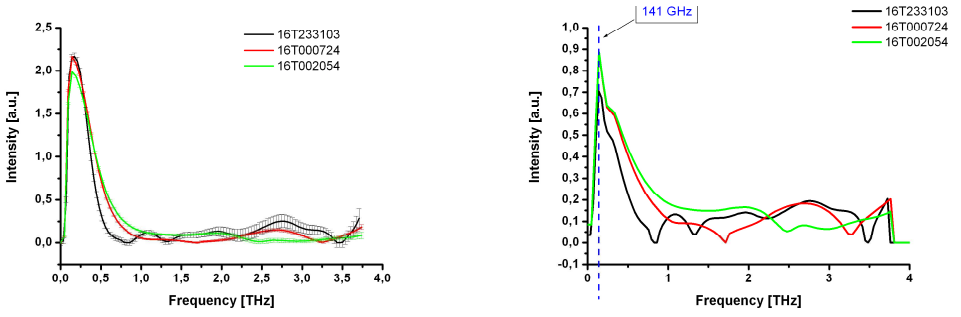

(a) CDR spectra during SASE operation (b) Bunch form factor during SASE operation

Figure 4.19: Measurements during SASE operation.

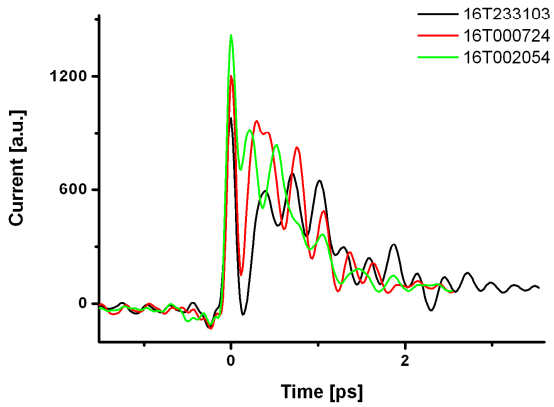

Figure 4.20: Bunch profile.

4.3 Conclusions

The longitudinal dimension of the electron bunch and its dependence on the RF accelerating phase have been studied taking into account that the compression of the bunch depends on its energy chirp, whose slope is in turn dependent on the RF phase. Different phases will then produce different stages of compression.

The measurements show a clear dependence of the bunch length on the accelerating phase as also expected from the phase scan (Fig. 4.5), whereas the same dependence is not evident in other measurements using different sources and devices (see [40], [44]).

The measured spectra have been corrected by the interferometer acceptance, quartz vacuum window and Golay cell frequency response in order to minimize the contribution of systematic errors.

The measured beam profiles, in good agreement with simulations and different measurements, present a sharp, asymmetric peak at high frequency and a long tail at low frequency. The curves are fitted with the function describing the true TTF profile and introduced in section 4.1.1. In case of shortest bunch (ACC1 on crest and ACC2-3 phase at 12 *deg*), the fit gives a FWHM of 1.2 ± 0.1 *ps* in good agreement with what measured by [40] downstream from the first bunch compressor (BC2) using synchrotron radiation through a Martin-Puplett interferometer.

We can conclude that the electron bunch starting with an rms length of 7.3 *ps* is slightly compressed by BC2 by a factor less than 2 and shortened by a factor 5 by BC3 down to 0.8 *ps* rms.

Finally, a few measurements performed during FEL operation want to give not only a good evidence of the non-intercepting nature of DR diagnostics, but also of the non-perturbing feature expected by this technique.

Conclusions

An accurate beam diagnostics is mandatory in the next generation light sources which require ultra-high brilliant beams, the brilliance, being defined as $B = \frac{I}{\varepsilon_x \varepsilon_y}$, with I the peak current and $\varepsilon_{x,y}$ the transverse emittance.

In the present work, we focused our attention on the characterization of the longitudinal beam size, which is related to the peak current in inverse proportion, by means of a frequency domain technique.

The autocorrelation measurement of coherent diffraction radiation, performed on the DESY VUV-FEL with an electron beam of 0.3 nC charge and 380 MeV energy, has shown a clear dependence of the bunch length on the RF accelerating phase in agreement with the RF phase scan where the maximum intensity is detected at the phase of maximum compression, i.e. minimum bunch length. To reduce the systematic error, the spectra have been corrected by the theoretical transmission of the z-cut quartz vacuum window, the simulated interferometer acceptance and the calibrated detector response. At this regard, an accurate characterization of the Golay cell detector has been performed with three different methods in three different frequency ranges, showing an almost flat dependence on the frequency and extending its frequency response to the mm-region. The corrected spectra have been therefore analyzed to retrieve the electron bunch profile from the bunch form factor, removing the ambiguity introduced by the missing phase factor by means of the Kramers-Kronig dispersion relation. The measured electron bunch profile is pulse shaped, a sharp peak with a long tail, whose minimum rms length is 0.8 ± 0.2 ps, in good agreement with simulations and bunch length measurements performed along the VUV-FEL with different techniques.

Several measurements during FEL operation have been taken to prove the effective non-intercepting and non-disturbing nature of diffraction radiation. As a result, the insertion of the screen with aperture either half or completely open does not affect the FEL generation process, allowing the longitudinal profile measurement to be performed parasitically.

Outlook

A Martin-Puplett interferometer, used to obtain the autocorrelation of coherent transition radiation from a silicon aluminate (SiAl) foil, will be placed in the SPARC hall right after the bunch compressor in June 2006. For this kind of measurement at SPARC, we plan to produce an upgraded version of the previous setup, front and top views are shown in Fig. 4.21. The interferometer will operate in Nitrogen controlled atmosphere and some mirrors will be assessed to be remote controlled in order to improve the alignment of the entire apparatus. Designs of the new setup are under study.

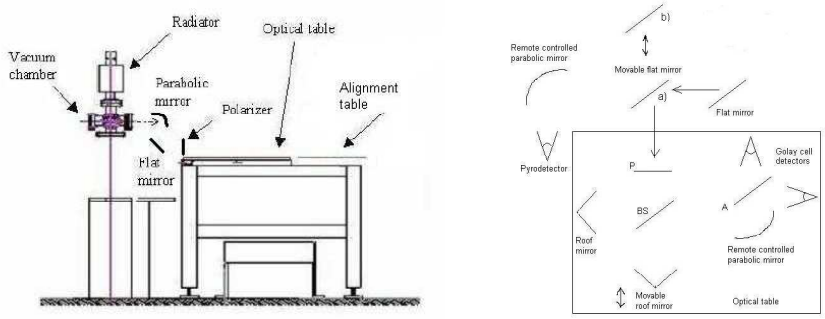

(a) Front-view (b) Top-view

Figure 4.21: Accelerating module phase scan.

The Martin-Puplett interferometer transfer function has been calculated also in the SPARC conditions, i.e. 155 MeV electron beam energy and transition radiation source, but using the same interferometer settings. The interferometer cut-off is evident in Fig. 4.22 at 150 GHz, in good agreement with what found experimentally (section 4.2.2).

As regard the Golay cell detector, it would be interesting to complete the hot-cold calibration with few more bandpass filter in the region of great

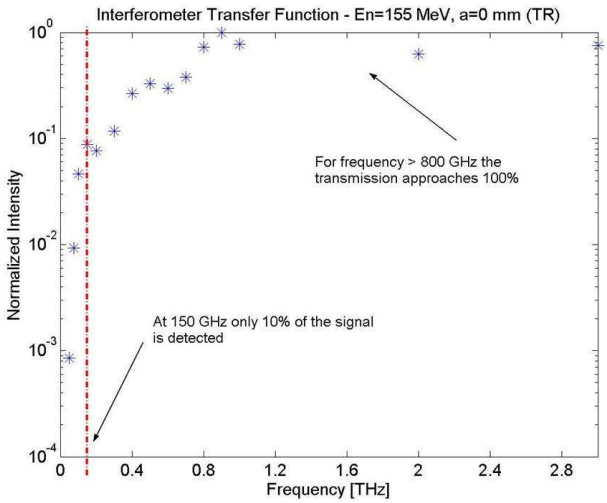

Figure 4.22: SPARC interferometer transfer function simulated with THz-Transport Code. Wire grids are treated as apertures. $E_{ebeam} = 155\ MeV$, transition radiation source.

interest for the bunch length measurement, that is between 200 Ghz and 800 GHz.

Appendix A

TTF VUV-FEL & SPARC Parameters

	Units	6.4 nm	30 nm
Electron beam			
Energy	MeV	1000	461.5
Peak current	kA	2.5	
rms bunch length	μm	50	
Bunch separation	ns	111	
Repetition rate	Hz	10	$2-5$
Normalized rms emittance	$\pi\ mm\ mrad$	2	
rms beam size	μm	68	100
rms energy spread	MeV	1	
Undulator			
Period	cm	2.73	
Gap	mm	12	
Peak magnetic field	T	0.495	
Coherent radiation			
Wavelength	nm	6.4	30
Saturation length	m	26.2	17.8
Peak power	GW	2.8	1.8

Table A.1: TTF VUV-FEL short wavelength mode of operation and current mode of operation.

	Units	500 μm
Electron beam		
Energy	MeV	155
Bunch Charge	nC	1.1
rms bunch length @ linac exit	mm	1
Bunch separation	ns	111
Repetition rate	Hz	$1 - 10$
Normalized rms transverse emittance	$\pi\ mm\ mrad$	< 2
rms beam size	μm	400
rms energy spread	MeV	0.3
Undulator		
Period	cm	2.8
Gap	mm	9
Coherent radiation		
Wavelength	μm	500
Saturation length	m	15
Peak power	GW	?

Table A.2: SPARC operation parameters.

Appendix B

Transparency of Millimeter Wave Materials

In the design of optical system for millimeter and sub-millimeter wavelength range the choice of the most suitable material is a critical issue. Diamond is the only material transparent in almost the whole spectral range, except for two absorption peaks at 5 μm and 20 μm. However, being diamond extremely expensive, various plastic materials with suitable properties are available. The choice of materials depends on losses, dielectric constants and suitability for ultra-high vacuum (UHV) applications. The window in the vacuum chamber has to be not only transparent to FIR radiation, but also such that its dimensions (viewing diameter and thickness) are capable to sustain the force exerted by atmospheric pressure. The optimum balance between transparency and UHV compatibility is given by crystalline quartz cut along the z-axis [**?**]. Except for a strong absorption peak at 78 μm, the transmission is almost constant (between 0.6 and 0.7) up to 8 mm as depicted in figure B.1.

One of the main problems in the wavelength range of interest is due to the water absorption lines. For this reason, it is worthwhile to operate in vacuum or in Nitrogen controlled atmosphere.

The low-resolution (interference free) transmission for normal incidence is calculated from the extinction coefficient k, the refractive index n and the

thickness d as [45]

$$T = \frac{(1 - R_0)^2 e^{-4\pi kd/\lambda}}{1 - R_0^2 e^{-8\pi kd/\lambda}} \tag{B.1}$$

where $R_0 = \frac{(1-n)^2+k^2}{(1-n)^2+k^2}$ is the single surface reflectivity. The transmittance curves for the most suitable materials in the millimeter and sub-millimeter wavelength range and for humid air are shown in figure B.1. The data source for all materials except diamond is reference [46].

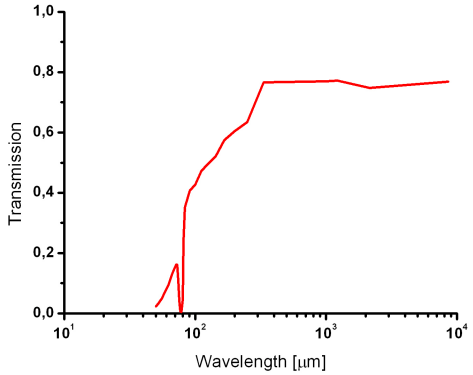

(a) Crystalline quartz

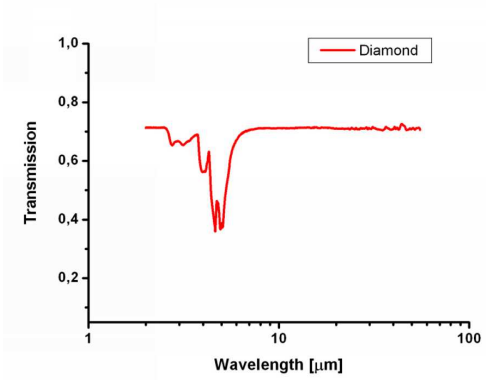

(b) Diamond

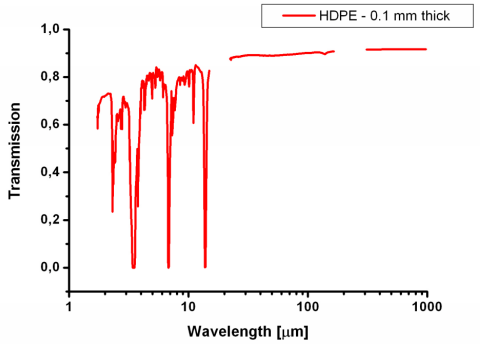

(c) HDPE

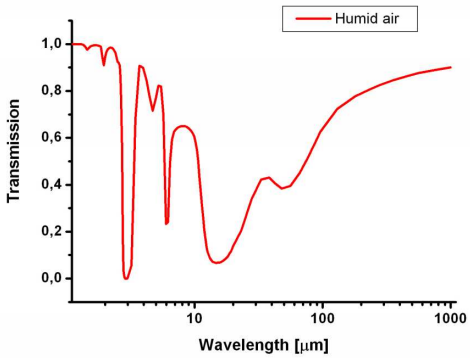

(d) humid-air

Figure B.1: Low-resolution (interference free) transmission curve for normal incidence.

Appendix C

Detector Calibration: Details

Instruments to calibrate our detector and the related components (attenuator and custom tapered waveguide) in the long wavelength range are vector and scalar network analyzers; the former are capable of measuring complex (amplitude and phase) reflection and transmission, while the latter can only measure amplitudes.

The scalar network analyzer (SNA), which directly drives a millimeter-wave source module to 110 GHz in waveguide, has been used to produce monochromatic, linearly polarized radiation[1], propagating through a set of three waveguides. The waveguides are built such that only the fundamental mode TE_{10} can propagate within the frequency band 75 - 110 GHz. Each waveguide is equipped with a directional coupler (DC) which has three output ports: the two main ports have a 1 to 1 coupling and the third one, isolated from the second one, is weakly coupled, in the specific case 10 dB, to one of the two main output ports. The third port of the first waveguide module extract about 10% of the oscillator power, to be used as a feedback system, and one of the two main ports feeds a ferrite isolator, which allows power to travel in one direction only. The following directional couplers feed the scalar network analyzer (HP 8757D) and are used to pick up the signal, part (10%) coming from the source (channel A) and part coming in the opposite direction (channel B). Channel A is used as a reference signal for the normalization of the output power, while channel B detects the reflected power and depends on the optics between the source and the detection system. In figure C.1 a schematics drawn of the experimental setup is shown. A chopper to modulate

[1]Collaboration with the University of Milano-Bicocca, Department of Physics.

the CW radiation is inserted between the isolator and the second waveguide, resulting in the interruption of the transport line. A horn antenna is therefore needed to collect radiation on the second waveguide. The common part ends with a variable attenuator necessary to limit the amount of power on the detector. After that two different end components can be added, as shown in figure C.1: a powermeter to calibrate the network analyzer and to evaluate the attenuation due to the optics, that is waveguides, couplers and attenuator, or the custom tapered waveguide directly attached to the Golay cell detector to characterize the detector frequency response.

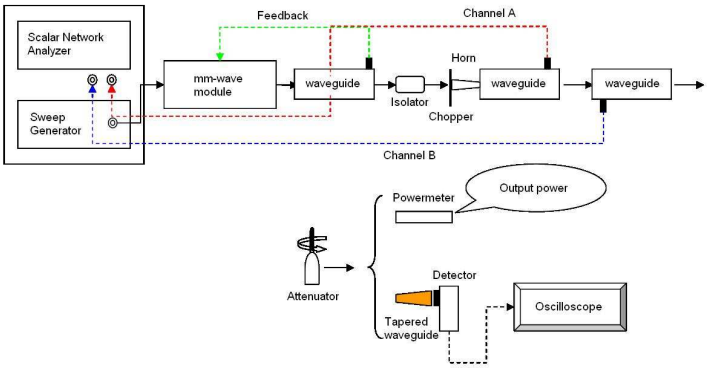

Figure C.1: Optimized Golay cell calibration setup

The network analyzer calibration is needed to know the effective output power which, in principle, in the ideal configuration of perfect optical coupling, that is without chopper, reaches the detector. Actually, since both a chopper and a horn antenna are inserted and the transport line open, the network analyzer calibration will give an estimation of the effects on both signal attenuation and frequency dependence.

C.1 Network Analyzer and Attenuator Calibration

The first step is the calibration of the scalar network analyzer output power. In order to get both a clear output signal and an output power incident on the Golay cell detector consistent with the power it can sustain, we selected

four values of power from the source, $-20\ dBm$, $-15\ dBm$, $-10\ dBm$ and $0\ dBm$. Eight frequencies in the $75-110\ GHz$ bandwidth have been selected and for each frequency the power has been recorded from both the analyzer (Fig. C.2*a)*), the value being given by the set initial power attenuated by the propagation in waveguides, and from the powermeter in the configuration *b)* of figure Fig. C.2 to check the attenuation factor due to the propagation in the waveguide.

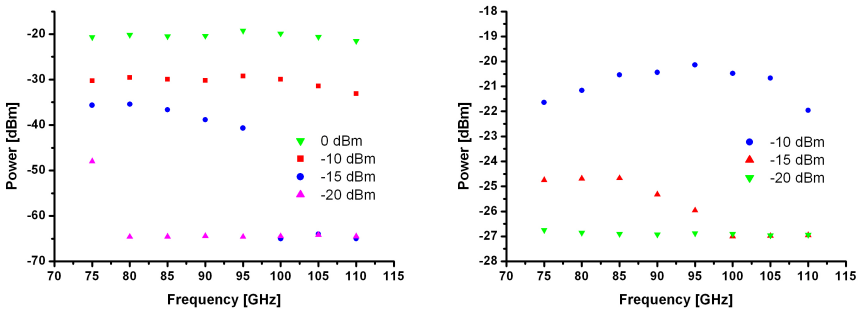

(a) Network analyzer reading (b) Powermeter measurement

Figure C.2: Source power spectrum for four different initial values of power.

From data a mean attenuation of $-9.6\ dB$ in the power source is detected at $-10\ dBm$ due to the waveguides. This value is a good estimation of the attenuation due to the optics, that is waveguides and couplers and it will be the correction factor of the source power in the Golay cell calibration calibration.

The initial source power has been set at $0\ dBm$, because the lower the initial power, the worst the analyzer response is, as figure C.2*a)* shows. However, even though attenuated by a factor of roughly $10\ dBm$, the power is still too high for the detector safety, being $10\ \mu W$ the maximum input power it can receive. An attenuator is then needed and its calibration, which provides the S_{ij}-elements of the scattering matrix has been performed with a vector network analyzer in the configuration shown in Fig. C.3.

The vector network analyzer has been calibrated first by measuring the total reflected power in the two local oscillators, S_{11} (S_{22}) by i) attaching a wave-guide short on 1 (2) (referred to Fig. C.3), ii) inserting a $\lambda/4$ delay line followed by a short in order to get the phase of the back-scattered wave changed by π, iii) closing 1 (2) with an absorber to simulate an adapted dummy load to measure the residual power. Ports 1 and 2 have then been directly connected to measure the transmitted power travelling from 1 to 2, S_{21}, and viceversa, S_{12}. From data, S_{12} and S_{21} result to be almost identical

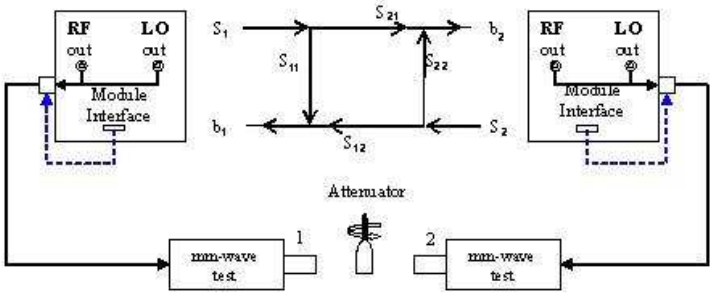

Figure C.3: Attenuator calibration apparatus setup.

with variations within $\pm 0.03\ dB$. The attenuator has then been inserted as shown in the scheme above (Fig. C.3) and a minimum attenuation of $0.2\ dB$ measured. The power, calculated as the square absolute value of S_{ij}, is a dimensionless quantity since it is the ratio to the reference power. The fraction of power signal absorbed by the dielectric is given by Eq. C.1

$$A_{12} = 1 - |S_{12}|^2 - |S_{11}|^2 \quad \text{(C.1)}$$

$$A_{21} = 1 - |S_{21}|^2 - |S_{22}|^2 \quad \text{(C.2)}$$

Figure C.4 shows three measurements for the maximum attenuation. The calibration gives an almost flat curve, variations being within $\pm 0.03\%$.

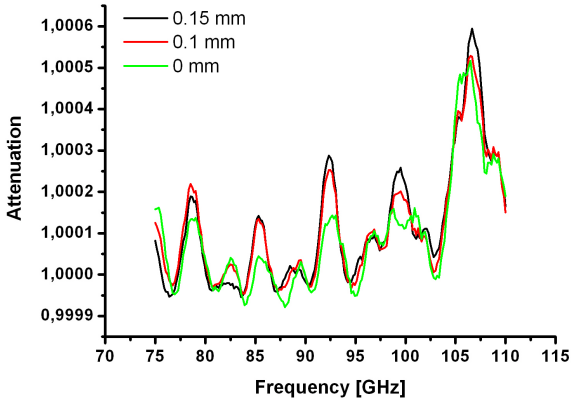

Figure C.4: Attenuation curves for the maximum attenuation.

C.2 Study and Realization of Tapered Waveguides

To reduce the power losses and the frequency dependent effects due to the insertion of the chopper, a tapered waveguide, shown in figure C.1 (orange cone), has been studied and built to have a standard flange with rectangular aperture ($x = 2.54\ mm$, $y = 1.27\ mm$) to ensure a perfect RF coupling with the last waveguide, an anticorodal conical tapered waveguide with aperture less than 30 deg and a custom circular flange with radius of 3 mm to match the detector window and avoid power losses. Simulations to foresee and evaluate reflected and transmitted power and to ensure, in the technical design, the transmission of the fundamental mode have been performed by using the HFSS simulation tool. In fact, due to the complicated geometry, the TE_{10} mode is not the only one propagating in such structure, higher order modes propagate as well, but we can assume the power losses due to the overmoding nature negligible, confirmations being given also by the tapered waveguide calibration. The inner surface rugosity is within 1.6 μm, peak-to-peak. The surface finish is opaque, but this does not affect the rugosity and it can be partially cleaned by using an "ultrasonic cleaner".

Two complementary waveguides have been built and both calibrated in the configuration shown in figure C.5 to evaluate losses and frequency dependence due to either overmoding or rugosity.

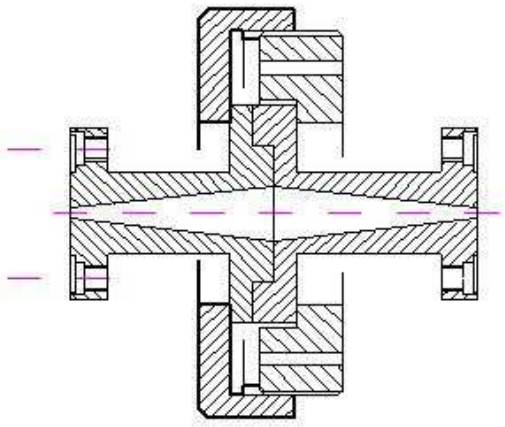

Figure C.5: Technical design of the tapered waveguides in the calibration configuration.

C.2.1 Tapered Waveguides Calibration

A vector and scalar network analyzer have been used to characterize the tapered waveguides and both Golay cell detectors. First we have calibrated the VNA (Agilent HP 8510C) by means of a short, open and load. The two complementary waveguides have been put in contact and the matrix scattering elements S_{11}, S_{21}, S_{12}, S_{22} measured, the RF contact being provided by a pair of clips, as shown in figure C.6.

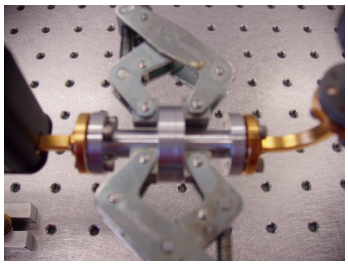

Figure C.6: Picture of the tapered waveguides in the calibration configuration.

The data show the transmitted power increases and the frequency dependence becomes flatter when the waveguides, in the configuration shown in the previous picture, are equipped to provide a good RF coupling. Figure C.7 shows the transmission coefficient for different solutions of RF contacts. As far as the RF contact is optimized, the transmission coefficient is improved reaching more than 95% (green curve) of the source power, with absorption peaks uniformly spaced with a period of roughly 3 GHz, corresponding to the total length of both waveguides, $L_{tot} = 45\ mm$, in the configuration of figure C.6. The peaks can be explained as resonances developed in the two coupled waveguides which act as a resonant cavity.

By looking at the data in the time domain it is straightforward to detect and accurately locate discontinuities in the waveguide. By selecting a portion of the spectrum, it is possible to estimate the losses due to the tapered waveguides and neglect effects coming from the experimental setup. Figure C.8 shows two reflection peaks separated by 0.3 nC which corresponds to discontinuities due to the interface between the tapered waveguide and the standard waveguide.

Except for periodic reflections due to the discontinuity at the interface between the two waveguides, a good transmission higher than 80% is shown. For the detector calibration a better RF contact between the tapered waveguide and the detector window has been established and by measuring the

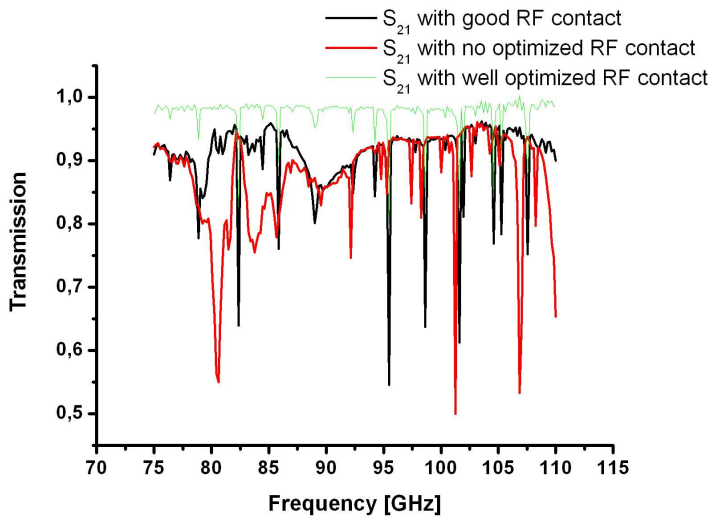

Figure C.7: Tapered waveguides transmission coefficient for different RF contact

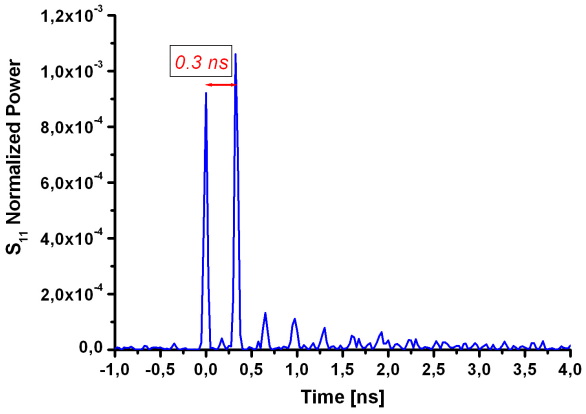

Figure C.8: Tapered waveguides transmission coefficient for different RF contact

power coming out from the tapered waveguide, neither attenuation nor strong frequency dependence has been observed as confirmed by figure C.9 which shows the source power measured with the powermeter located right after the last waveguide (black curve), the attenuator (red curve) and the two tapered waveguides in the calibration configuration (green curve).

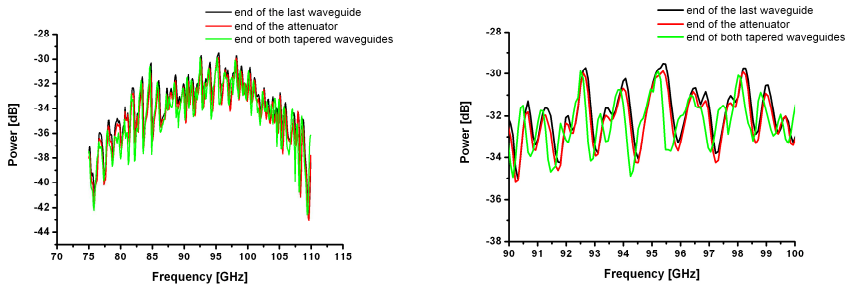

(a) (b) zoom-in

Figure C.9: Source power spectrum at the end of each component constituting the transmission channel.

Figure C.9b) is the detailed image, showing a slight (0.3 GHz) backshifting in frequency due to the tapered waveguides, but no sensitive power attenuation is detected.

Appendix D

Fourier Transform Spectroscopy

The principles of Fourier transform spectroscopy were discovered by Michelson and Rayleigh, who found out how the interference pattern from a two-beam interferometer, obtained by altering the path difference between the two beams, is the Fourier transform of the radiation passing through the interferometer.

Consider a vertically polarized plane wave with the wave vector $\vec{k}$ which produces an incident electric field given by

$$\vec{E}(t,\vec{r}) = E_0 \sin(\omega t - \vec{k}\cdot\vec{r})\hat{u}_v \tag{D.1}$$

at the beam splitter, $\hat{u}_v$ being the vertical unit vector; $\vec{k}\cdot\vec{r}$ is a constant phase which can be neglected. Since the beam divider has wires placed at 45^o when viewed along the input beam axis, the incident electric field will be split in a reflected field $\vec{E}_r$ and a transmitted field $\vec{E}_t$ such that

$$\begin{aligned} \vec{E}_t(t) &= \frac{E_0}{\sqrt{2}}\sin(\omega t)\frac{\hat{u}_h + \hat{u}_v}{\sqrt{2}} \\ \vec{E}_r(t) &= \frac{E_0}{\sqrt{2}}\sin(\omega t)\frac{\hat{u}_h - \hat{u}_v}{\sqrt{2}} \end{aligned} \tag{D.2}$$

At the roof mirrors, the $\hat{u}_h + \hat{u}_v$ component will then be reflected with its plane of polarization altered to $\hat{u}_h - \hat{u}_v$ and similarly the $\hat{u}_h - \hat{u}_v$ component will change into $\hat{u}_h + \hat{u}_v$ upon reflection.

As the moveable mirror is moved, producing a path length difference, $2\Delta x$, between the two beams, the electric field components will go back to the polarizing beam splitter differing by a phase factor $\tau = \frac{2\Delta x}{c}$ as given by Eq. D.3

$$\begin{aligned} \vec{E}_t'(t) &= \vec{E}_t(t-\tau) = \frac{E_0}{\sqrt{2}}\sin(\omega(t-\tau))\frac{\hat{u}_h + \hat{u}_v}{\sqrt{2}} \\ \vec{E}_r'(t) &= \vec{E}_r(t) = \frac{E_0}{\sqrt{2}}\sin(\omega t)\frac{\hat{u}_h - \hat{u}_v}{\sqrt{2}} \end{aligned} \tag{D.3}$$

The reflected and transmitted components recombine to produce a total field, $\vec{E}_f = \vec{E}_r' + \vec{E}_t'$, at the analyzer which can be written by using trigonometric addition formulas as

$$\vec{E}_f(t) = E_0\Big[\sin\Big[\omega\Big(t-\frac{\tau}{2}\Big)\cos\Big(\frac{\omega\tau}{2}\Big)\Big]\hat{u}_h + \tag{D.4}$$

$$+ \sin\Big(\frac{\omega\tau}{2}\Big)\cos\Big[\omega\Big(t-\frac{\tau}{2}\Big)\Big]\hat{u}_v\Big] \tag{D.5}$$

The horizontal and vertical components are 90^o out of phase and the amplitudes depend on the phase difference, $\omega\tau$, resulting in an elliptically polarized radiation.

Assuming a source with an arbitrary intensity distribution, $I(\omega)$, the intensity of the recombined radiation at the detectors can be written as [40]

$$V_{h,v} \propto \int_{-\infty}^{\infty} (\vec{E}_f \cdot \hat{u}_{h,v})^2 dt \tag{D.6}$$

which becomes

$$\begin{aligned} V_h(\tau) &\propto \int_0^{\infty} I(\omega)\cos^2(\frac{\omega\tau}{2})d\omega \\ V_v(\tau) &\propto \int_0^{\infty} I(\omega)\sin^2(\frac{\omega\tau}{2})d\omega \end{aligned} \tag{D.7}$$

The normalized difference interferogram then can be written as

$$\begin{aligned} \delta(\tau) &= \frac{\int_0^{\infty} I(\omega)(\cos^2(\frac{\omega\tau}{2}) - \sin^2(\frac{\omega\tau}{2}))d\omega}{\int_0^{\infty} I(\omega)(\cos^2(\frac{\omega\tau}{2}) + \sin^2(\frac{\omega\tau}{2}))d\omega} \\ &= \frac{\int_0^{\infty} I(\omega)\cos(\omega\tau)d\omega}{\int_0^{\infty} I(\omega)d\omega} \end{aligned} \tag{D.8}$$

being the Fourier cosine transform of the radiation spectrum. Since $\delta(\tau)$ is the measured quantity, the frequency spectrum of the incident radiation pulse

can be obtained by inverse Fourier transforming the normalized difference interferogram as given by Eq. D.9

$$I(\omega) = \int_{-\infty}^{\infty} \delta(\tau) \cos(\omega\tau) d\tau \tag{D.9}$$

In the data evaluation, the continuous transform is replaced by a discrete one (Eq. D.10), since data extend over a finite time interval, depending on the roof mirror excursion

$$I(\omega_k) = \frac{1}{N} \Re \sum_{n=1}^{N} \delta(\tau_n) \exp(i\omega_k \tau_n) \tag{D.10}$$

N being the number of data points.

Bibliography

[1] F. Richard *et al.* (eds.), *TESLA Technical Design Report*,March 2001, DESY-2001-011

[2] LCLS Conceptual Design Report - `www-ssrl.slac.stanford.edu/lcls/cdr`

[3] SPARC Group (LNF-INFN, Roma1-INFN, Roma2-INFN, ENEA, CNR, Milano-INFN), *Technical Design Report*, January 2004 - `www.lnf.infn.it/acceleratori/sparc/`

[4] `www.linearcollider.org`

[5] H. Lihn *et al.*, *Measurement of subpicosecond electron pulse*, Physical Review E (**53**), n.6 - 1996

[6] E. Chiadroni, *Studio e sviluppo di un laser ad elettroni liberi a singolo passaggio nella regione spettrale dei raggi X*, Master Thesis - a.a. 2001-2002 - Univ. degli Studi di Roma "La Sapienza"

[7] E.L. Saldin, E.A. Schneidmiller, M.V. Yurkov, *The Physics of Free-Electron Lasers*, Springer, Berlin-Heidelberg (2000)

[8] *SASE FEL at the TESLA Facility, Phase 2*, DESY-TESLA-FEL-2002-01

[9] Coherent Radiation Diagnostics: `http://tesla.desy.de/fla/crd/crd.html`

[10] S. Casalbuoni *et al.*, *Numerical Studies on the Electro-Optical Sampling of Relativistic Electron Bunches*, TESLA Report 2005-01

[11] R. Lai *et al.*, Phys. Rev. E **50**, 4294 (1994)

[12] G. Orlandi, *Misura della lunghezza del pacchetto di elettroni dell'acceleratore lineare superconduttivo TTF (Tesla Test Facility) con la radiazione di transizione e diffrazione*, PhD Thesis - University of Rome "Tor Vergata", 1999

[13] J.H. Brownell, G. Doucas, *Role of the grating profile in Smith-Purcell radiation at high energies*, Phys. Review ST - Accelerators and Beams, (**8**), 091301 (2005)

[14] J.D. Jackson, *Classical Electrodynamics*, Third Edition, J.Wiley & Sons, Inc.

[15] M. Castellano, A. Cianchi, G. Orlandi, V. Verzilov, Nucl. Instr. and Meth. in Phys. Res. A 435, pp. 297-307, 1999

[16] M.L. Ter-Mikaelian, *High-Energy Electromagnetic Processes in Condensed Media*, Wiley-Interscience

[17] C. Bernardini, O. Ragnisco, P.M. Santini, *Metodi Matematici della Fisica*, La Nuova Italia Scientifica

[18] M.Born, E. Wolf, *Principles of optics*, Pergamon Press, 1965

[19] R. Lai, A.J. Sievers, *On using the coherent far IR radiation produced by a charged-particle bunch to determine its shape: I Analysis*, NIM A **397** (1997) 221-231

[20] V. Verzilov, *Transition Radiation in the Pre-Wave Zone*, SIS-Pubblicazioni LNF-99/018(p), 1999

[21] P. Michelato *et al.*, *Cs_2Te photocathode for the TTF Injector II*, EPAC 96, THP068L

[22] D.H. Dowell, P. G. O'Shea, *Coherent Synchrotron Radiation Induced Emittance Growth in a Chicane Buncher*, Proceedings of the Particle Accelerator Conference, Vancouver 1997

[23] M. Krasilnikov *et al.*, *Optimizing the PITZ electron source for the VUV-FEL*, EPAC 2004, Luzern, Switzerland, July 5-9, 2004

[24] K. Honkavaara, *Commissioning of the TTF Linac Injector at the DESY VUV-FEL*, Proceedings of the 2004 FEL Conference, 371-374

[25] A. Loulergue, A. Mosnier, *A Simple S-Chicane for the Final Bunch Compressor of TTF-FEL*, Proceedings of EPAC 2000, Vienna, Austria

[26] G. Grygiel *et al.*, *DOOCS: A Distributed Object- Oriented Control System on PC's and Workstations*, PCaPAC conference, 1996 - `http://tesla.desy.de/doocs/doocs.html`

[27] M. Sparks, E. Loh, *Temperature Dependence of the Absorptance in Laser Damage of Metallic Mirrors, part I-II*, J. Opt. Soc. Am. (**69**), 847-868 (1979)

[28] J.W. Lamb, *Miscellaneous Data on Materials for Millimetre and Submillimetre Optics*, Private Note

[29] D.H. Martin, E. Puplett *Polarised Interferometric Spectrometry for the Millimetre and Submillimetre Spectrum*, Infrared Physics (**10**), pp. 105-109 (1970)

[30] J.C.G. Lesurf, *Millimeter-wave optics, devices and systems*, Adam Hilger, January 1990

[31] S. Casalbuoni, R. Ischebeck, *Simulation of Wave Front Propagation with ZEMAX*, DESY - FLA Seminar talks - `http://tesla.desy.de/fla/publications/talks/seminar/seminar.html`

[32] L. Fröhlich, O. Grimm, *Bunch Length Measurements Using a Martin-Puplett Interferometer at the VUV-FEL*, Proceedings of the FEL 2005, Stanford, August 20-26, 2005

[33] H.A. Zahl, M.J.E. Golay, *Pneumatic Heat Detector*, The Review of Scientific Instruments, **17**, No.11 (1946)

[34] `www.terahertz.co.uk/QMCI/Golay/Diamond_Golay_Manual.pdf`

[35] E. Chiadroni, H. Delsim-Hashemi, L. Fröhlich, O. Grimm, *Detector response and beam line transmission measurements with far-infrared radiation at TTF2*, Proceedings of the FEL 2005, Stanford, August 20-26, 2005

[36] P. De Bernardis, *Tecniche sperimentali in astrofisica*, `www.phys.uniroma1.it/DipWeb/web_disp/d5/index.html`

[37] R. Ulrich, *FIR Properties of Metallic Mesh and its Complementary Structure*, Infrared Physics, **7**, n.1 (1967)

[38] M.F. Kimmitt, *Far-Infrared Techniques*, ed. H.J. Goldsmid

[39] M.Cuisenier, A. Marten, J. Mondellini, *Interferometres de Fourier dans l'infrarouge lontain et le submillimetrique. Etude comparative de leurs performances en vue d'applications spatiale*, J. Optics (Paris), 1992, (**23**), n.5, pp.179-198

[40] L. Fröhlich, *Bunch Length Measurements Using a Martin-Puplett Interferometer at the VUV-FEL*, DESY-THESIS 2005-011, June 2005

[41] J. Rosenzweig, A. Murokh, A. Tremaine, *Coherent transition radiation-based diagnosis of electron beam pulse shape*, 8^{th} Advanced Accelerator Concepts Workshop, 1999

[42] B. Steffen *et al.*, *Spectral Decoding Electro Optic Bunch Length and Arrival Time Jitter Measurements at the DESY VUV-FEL*, Proceedings of the FEL 2005, Stanford, August 20-26, 2005

[43] S. Schreiber *et al.*, *Performance of the TTF Photoinjector for FEL Opeartion*, Proceedings of the ICFA Workshop, Chia Laguna July 2002

[44] A. Bolzmann, *Investigation of the longitudinal charge distribution of electron bunches of the VUV-FEL using the transverse deflecting cavity LOLA*, Diploma Thesis - to be printed on DESY Notes

[45] P. Dore *et al.*, *Infrared properties of chemical-vapor deposition polycrystal;one diamond windows*, Applied Optics **37**, No. 24, p. 5731

[46] E.D. Palik (ed.), *Handbook of Optical Constants of Solids*

Thanks to...

...my mum, dad and Nicki, for being my daily support.

...my dear friends Adri, for sharing with me the last three years as a sister, and Clo, for being always there.

...Pietro Musumeci, the only one who makes me feel free of learning.

...Michele Castellano, whose explanations have always cleared to me many doubts. I unfortunately ask him few times.

...Sergio Tazzari who, extremely patient, has read and corrected every word of this thesis several times.

...Luciano Catani and Alessandro Cianchi, who trusted me and assisted me in setting the experiment up and during the many shifts.

...Victor Verzilov, who first introduced me to the THz world.

...Rossano Sorchetti who taught me something about technical design and mechanical construction, but mostly how to face tough questions with positivity and always smiling.

...Luciano Cacciotti for his support in electric circuits construction.

...David Alesini for his support in RF concerning topics.

...the LNF-building-four-ground-floor guys, Giancarlo, Massimo, Daniele, Carlo and Marco, for the time spent together.

...Massimo De Petris (Phys. Dept. of the University of Rome "La Sapienza") and Massimo Gervasi (Phys. Dept. of the University of Milano-Bicocca) and their groups for sharing knowledge, instrumentations and time with us.

...Paolo Dore for the pleasant discussions and first hints on Golay cells world.

...the Elettra-Sincrotrone Trieste people, in particular Carlo Bocchetta, Gerardo D'Auria and Mario Ferianis, for supporting this work with instrumentation (Golay cells are property of Elettra in the framework of SPARC collaboration) and funds.

...Jörg Roßbach and Peter Schmüser for giving me the opportunity to carry out my experiment at DESY.

...Oliver Grimm, whose personal and technical contribution has been essential to the success of this work.

...Sara Casalbuoni, who always supported me, both technically and friendly during the last two years in Hamburg and Elena, her daughter, who has been my best playing-mate.

...Lars Fröhlich, Hossein Delsim-Hashemi, Holger Schlarb, Bart Faatz and Dmytro Pugachov for sharing with me their knowledge and both their working and spare time.

...Katja Honkavaara, Gero Kube, Otto Peters, Reiner Fischer, Bernd Steffen, Bernhard Schmidt, Axel, Jan and all TTF operators for the technical support and for interesting discussions.

...Britta Redlich at FELIX for her assistance in preparing and carrying out the measurements and tests.

Ed infine, alla persona che è improvvisamente apparsa nella mia vita e l'ha stravolta, abbattendo le mie poche certezze per costruirne di nuove e più salde, grazie...